

**SYNTHESIS AND CHARACTERIZATION OF Mo-V-Nb-Te-O
M1 CATALYSTS**

by

Wenxin Wang

A thesis submitted to the Faculty of the University of Delaware in partial fulfillment of the requirements for the degree of Bachelor of Science in Chemical Engineering with Distinction

Spring 2017

© 2017 Wenxin Wang
All Rights Reserved

**SYNTHESIS AND CHARACTERIZATION OF MO-V-NB-TE-O
M1 CATALYSTS**

by

Wenxin Wang

Approved: _____
Douglas Buttrey, Ph.D
Professor in charge of thesis on behalf of the Advisory Committee

Approved: _____
Ismat Shah, Ph.D
Committee member from the Department of Materials Science and
Engineering

Approved: _____
Emily Day, Ph.D
Committee member from the Board of Senior Thesis Readers

Approved: _____
Hemant Kher, Ph.D.
Chair of the University Committee on Student and Faculty Honors

ACKNOWLEDGMENTS

It has been two years since I worked with Dr. Buttrey. There are many people I would like to acknowledge deeply, especially my advisor and first reader, Prof. Buttrey. He taught me on crystal structure analysis patiently and gave me a chance to gain hands on research experience. I also would like to thank Dr. Jerry Poirier for X-ray training. Also, special thanks to my second reader Prof. Ismat Shah and third reader Prof. Emily Days for helping me on my senior thesis and defense presentation. I also want to thank Sumeet Kothare and Brady Bowman, who have worked with me in Prof. Buttrey's group. Last but not least, I would like to thank my family and all my friends for support during past two years.

TABLE OF CONTENTS

LIST OF TABLES	vi
LIST OF FIGURES	viii
ABSTRACT	xii
CHAPTERS	
1 INTRODUCTION	1
1.1 Background Information	1
1.2 Mo-V-Nb-Te-O Mixed Metal Oxides	2
1.3 The Selectivity of Nb, Te	4
1.4 Research Objective	5
1.5 Future Path.....	5
2 METHOD	7
2.1 Synthesis Method	7
2.2 Characterization Methods.....	8
2.2.1 X-ray Diffraction	8
2.2.2 Bragg's Law	13
2.2.3 Pseudo-Voigt approximation.....	14
2.2.4 Instrumental Width.....	17
2.2.5 Scherrer Equation	21
2.2.6 Calibration	22
3 PRECALCULATION	23
3.1 Determining Mass Proportions of Reagents.....	23
3.2 Intensity Calculation.....	25
4 SYNTHESIS OF Mo-V-Nb-Te-O.....	28
4.1 Introduction	28
4.2 Experimental.....	28
5 DETERMINATION OF FACTORS INFLUENCING HABIT	32
5.1 Metal Ratio	32
5.2 Calcination Temperature under Argon Gas.....	41
5.3 Argon Calcination Time	51
5.4 pH of the solution	55

6	CONCLUSION	58
	REFERENCES	61
APPENDICES		
A	MORE CRYSTAL STRUCTURES AND X-RAY DIFFRACTION PATTERNS	66
	A.1 Mo-V-Nb-Te-O <i>M1</i> phase	66
	A.2 Mo-V-Nb-Te-O <i>M2</i> phase	67
	A.3 Mo5O14.....	69
B	MATLAB CODE	70
	B.1 Pseudo-Voigt approximation.....	70
C	FWHM FOR SILICON STANDARD	71

LIST OF TABLES

Table 2.2.1.1 Atomic coordinates and occupancies for all sites in the Mo-V-Nb-Te-O <i>MI</i> phase; space group <i>Pba2</i> (no.32); a=21.134(1) Å, b=26.647(1) Å, c=4.0140(2) Å; Z=4 ³	10
Table 2.2.1.2 Atomic coordinates and occupancies for all sites in the Mo-V-Nb-Te-O <i>M2</i> phase; space group <i>Pmm2</i> (no.25); a=12.6294(6) Å, b=7.2956(30) Å, c=4.02010(7) Å; Z=4 ⁹	12
Table 2.2.4.1 Miller indexes and scattering angles for NIST Silicon Standard Reference Material (SRM 640e) at 22.5°C using Cu K _{α1} radiation with λ = 0.15405929 nm and using lattice parameter a = 0.54311788(31) nm ¹⁰	18
Table 2.2.4.2 The instrumental width and crystal size (The width is indicated by the FWHM of intensity peaks of the silicon standard sample. The unit is in rad. The crystal size is calculated from Scherrer equation)	20
Table 3.1.1 The bond valence of each set element in <i>MI</i> phase.	24
Table 3.2.1 The multiplicity for powder diffraction data	26
Table 4.2.1 The ratio of the component metals in the mixture.....	29
Table 4.2.2 The calcination condition set up to analyze the effect of ratio, and argon calcination temperature	30
Table 4.2.3 The calcination condition set up to analyze the effect of argon calcination temperature and time	30
Table 4.2.4 The condition set up for the pH analysis.....	31
Table 5.1.1 The purity of the Mo-V-Nb-Te-O <i>MI</i> phase catalyst, indicated by the ratio of <i>M2/MI</i> , for all three metal ratio sample sets (High, Mo:V:Nb:Te = 1:0.31:0.14:0.27; medium, Mo:V:Nb:Te = 1:0.24:0.13:0.27; low, Mo:V:Nb:Te = 1:0.22:0.12:0.27. The high, medium, and low ratio were named by the ratio of V/Mo.).....	36
Table 5.1.2 The crystal sizes of the three metal ratio sample sets (High, Mo:V:Nb:Te = 1:0.31:0.14:0.27; medium, Mo:V:Nb:Te = 1:0.24:0.13:0.27; low, Mo:V:Nb:Te = 1:0.22:0.12:0.27. The high, medium, and low ratio were named by the ratio of V/Mo.).....	39

Table 5.2.1	The crystal sizes of the medium V/Mo ratio (Mo:V:Nb:Te = 1:0.24:0.13:0.27) sample sets	44
Table 5.2.2	The crystal dimensions of the high V/Mo ratio (Mo:V:Nb:Te = 1:0.31:0.14:0.27) sample sets	46
Table 5.2.3	The crystal sizes of the low V/Mo ratio (Mo:V:Nb:Te = 1:0.22:0.12:0.27) sample sets	47
Table 5.2.2	The correlation between crystallite dimensions and calcination temperature for the low-range metal ratio specimens.	50
Table 5.4.1	The result of whether <i>MI</i> phase was crystallized successfully from the pH analysis	56

LIST OF FIGURES

Figure 1.2.1	[001] projection of the Mo-V-Nb-Te-O <i>M1</i> structure.....	3
Figure 1.2.2	[001] projection of the Mo-V-Nb-Te-O <i>M2</i> structure.....	4
Figure 2.2.1.1	The X-ray diffraction pattern simulated from CrystalDiffract (software) for Mo-V-Nb-Te-O <i>M1</i> phase ($0^\circ < 2\theta < 80^\circ$)	11
Figure 2.2.1.2	The simulated X-ray diffraction pattern from CrystalDiffract for Mo-V-Nb-Te-O <i>M2</i> phase	13
Figure 2.2.2.1	The interpretation of Bragg's law.....	14
Figure 2.2.3.1	The comparison on the peak shapes from the pseudo-Voigt approximation, Gaussian distribution and Lorentzian distribution.	15
Figure 2.2.3.2	The measurement of the Bruker D8 Advance Diffractometer instrumental width.....	16
Figure 2.2.4.1	The expected X-ray diffraction profile from the NIST Si Standard SRM 640e ($5^\circ < 2\theta < 80^\circ$) (<i>hkl</i> on figures) using a Cu $K\alpha$ source. 19	
Figure 2.2.4.2	The (111) peak intensity from the NIST Si Standard SRM 640e showing an instrument-limited full width at half maximum of $0.227(2)^\circ$. This peak should be centered at 28.441° and can be used, along with other standard peak positions, to determine the systematic zero point correction for the instrument. Analysis must also account for the presence of a shoulder peak at 28.513° corresponding to the $K\alpha_2$ contribution, which has intensity that is half that of $K\alpha_1$	19
Figure 2.2.4.3	The instrumental width for Bruker D8 XRD in ISE lab.....	21
Figure 3.2.1	The calculated relative intensity of Mo-V-Nb-Te-O <i>M1</i> phase in the Bragg angle range $5^\circ < 2\theta < 55^\circ$ without peak profiles.	27
Figure 3.2.2	The calculated relative intensity of Mo-V-Nb-Te-O <i>M1</i> phase in the Bragg angle range $5^\circ < 2\theta < 55^\circ$ without peak profiles.	27
Figure 5.1.1	The X-ray diffraction pattern of metal ratio analysis at 575°C argon calcination temperature (2h argon calcination, XRD setting :4s, 0.02 degree per step, $\lambda=1.5406\text{\AA}$)	32

Figure 5.1.2 The X-ray Diffraction pattern of metal ratio analysis at 600°C argon calcination temperature (2h argon calcination, XRD setting :4s, 0.02 degree per step, $\lambda=1.5406\text{\AA}$)	33
Figure 5.1.3 The X-ray diffraction pattern of metal ratio analysis at 625°C argon calcination temperature (2h argon calcination, XRD setting :4s, 0.02 degree per step, $\lambda=1.5406\text{\AA}$)	33
Figure 5.1.4 Expanded section of the X-ray diffraction pattern for the low metal ratio under 625°C argon calcination temperature, selected to show the <i>M2</i> phase contaminant. (The intense peak with question mark is (220) peak for <i>M2</i> phase structure, and the ratio of <i>M2</i> / <i>M1</i> phase was calculated based on that and (001) peak for ratio of <i>M1</i> phase.).....	34
Figure 5.1.5 The example of X-ray diffraction pattern fit for the low metal ratio under 625°C argon calcination temperature.....	35
Figure 5.1.6 The influence of metal ratio on the <i>M2</i> / <i>M1</i> ratio under different calcination temperatures.....	36
Figure 5.1.7 The X-ray Diffraction pattern at low angle range for the low metal ratio under 600°C argon calcination temperature to show the crystal size was found on each axis. (b-axis as a sample calculation; XRD setting: 60s 0.01 degree per step, $\lambda=1.5406\text{\AA}$)	38
Figure 5.1.8 The influence of metal ratio on the crystal thickness along different directions for the samples calcinated at 575°C	39
Figure 5.1.9 The influence of metal ratio on the crystal thickness along different directions for the samples calcinated at 600°C	40
Figure 5.1.10 The influence of metal ratio on the crystal thickness along different directions for the samples calcinated at 625°C.....	40
Figure 5.1.11 The ratio of <i>c</i> -axis to basal plane crystal dimensions for different V/Mo under different calcination temperatures. The inset prisms depict the relative changes in crystallite morphology.	41
Figure 5.2.1 The X-ray diffraction pattern of the medium V/Mo ratio sample set (2h argon calcination, XRD setting: 4s, 0.02 degree per step, $\lambda=1.5406\text{\AA}$).....	42
Figure 5.2.2 The trends of <i>M2</i> / <i>M1</i> ratio change with the change of the calcination temperatures for different V/Mo ratio	43

Figure 5.2.3	The influence of argon calcination temperature change on the crystal thickness along different directions for the medium V/Mo ratio sample set.....	44
Figure 5.2.4	The <i>MI</i> phase crystal size and shape change by temperature for different V/Mo ratio sample sets	45
Figure 5.2.5	The X-ray diffraction pattern of the high V/Mo ratio sample set (2h argon calcination, XRD setting: 4s, 0.02 degree per step, $\lambda=1.5406\text{\AA}$) ..	45
Figure 5.2.6	The X-ray diffraction pattern of the low V/Mo ratio sample set (2h argon calcination, XRD setting: 4s, 0.02 degree per step, $\lambda=1.5406\text{\AA}$) ..	47
Figure 5.2.7	The influence of argon calcination temperature change on the crystal thickness along different directions for the low V/Mo ratio sample set.	48
Figure 5.2.8	Sequence of XRD patterns from the various argon treatment temperatures (2h argon calcination, XRD setting: 4s, 0.02 degree step size at $\lambda=1.5406\text{\AA}$).	48
Figure 5.2.9	HAADF-STEM image at 80 kV showing the HTB-type pseudo-hexagonal <i>M2</i> domain bounded by a region with substantial disorder within which pentagonal building blocks are found, some of which are conjoined as pairs, triplet, and quadruplets, as marked in yellow. ²³	50
Figure 5.2.9	The influence of argon calcination temperature on the crystallite dimensions.	51
Figure 5.3.1	The X-ray diffraction pattern of the argon calcination time analysis (argon calcination at 625°C, XRD setting: 4s, 0.02 degree per step, $\lambda=1.5406\text{\AA}$).....	52
Figure 5.3.2	The influence of calcination time on the crystal thickness along different directions (calcination $T = 625^\circ\text{C}$).	53
Figure 5.3.3	The <i>MI</i> crystallite size and shape dependence on calcination time at $T = 625^\circ\text{C}$	53
Figure 5.3.4	The trends of <i>M2/MI</i> ratio with increasing calcination time at $T = 625^\circ\text{C}$	54
Figure 5.3.5	The comparison of longer calcination time under 500°C argon calcination temperature (XRD setting: 4s, 0.02 degree per step, $\lambda = 1.5406\text{\AA}$).....	54

Figure 5.4.1	The X-ray diffraction patterns from the pH dependent study (2h argon calcination at 600°C, XRD setting: 4s, 0.02 degree per step, $\lambda=1.5406\text{\AA}$).....	57
Figure A.1.1	The X-ray diffraction pattern from CrystalDiffract for Mo-V- Nb-Te-O <i>MI</i> phase ($0^\circ < 2\theta < 180^\circ$)	66
Figure A.1.2	[001] bond structure of the Mo-V-Nb-Te-O <i>MI</i> phase catalyst (with labels)	67
Figure A.2.1	[001] bond structure of the Mo-V-Nb-Te-O <i>MI</i> phase catalyst (with labels)	68
Figure A3.1	The X-ray diffraction pattern from CrystalDiffract for Mo5O14 ($0^\circ < 2\theta < 80^\circ$).....	69
Figure C.1	The zoom in intensity plot with FWHM at 47.300° ($hkl=220$).....	71
Figure C.2	The zoom in intensity plot with FWHM at 56.120° ($hkl=311$).....	72
Figure C.3	The zoom in intensity plot with FWHM at 69.126° ($hkl=400$).....	72
Figure C.4	The zoom in intensity plot with FWHM at 76.372° ($hkl=331$).....	73

ABSTRACT

Mo-V-Nb-Te-O mixed metal oxides are the most efficient catalysts for new alkane-fed processes leading to some important C2 and C3 compounds in the chemical industry, such as ethylene, acrylic acid and acrylonitrile [1]. The purpose of this research is to study factors influencing the morphology of the orthorhombic *MI* phase catalyst. Control of the crystallite dimensions of the desired catalyst phase, *MI*, requires control of composition and impurity phase content. The *MI* phase was synthesized by mixing ammonium vanadate, ammonium heptamolybdate, telluric acid, and ammonium niobium oxalate in sequence, similar to a procedure used earlier by PhD student Xin Li [2,3]. The *MI* phase was observed for calcination temperatures between 575°C and 625°C and for several starting compositions. The lower V/Mo ratios, longer calcination times, or close proximity to the limits of calcination temperature produced higher-purity crystalline *MI* phase, as long as all conditions fall within reasonable ranges. Higher calcination temperatures resulted in increased crystal size along the *c*-axis. One of our goals is to obtain crystallites with small dimension along *c*-axis, but large dimensions perpendicular to *c*-axis, since the catalytically active surface is oriented perpendicular to *c*-axis. For this reason, reducing the *c/ab*_average ratio is a priority. Under the same element ratio, pH, and argon calcination time, 550°C argon calcination is found to be near optimal to approach the goal. For temperatures below 500°C, for the calcination temperature, the Mo-V-Nb-Te-O mixed metal oxides did not crystallize very well. The pentagonal ring building-blocks found in the *MI* phase do not fully self-assemble if the calcination temperature is too low or if there is insufficient time for growth; they exist only as disordered clusters [4]. These disordered products are much less active than the well-ordered

orthorhombic *M1* phase. Increasing the calcination time up to 96h for this sample did not result in a well-ordered orthorhombic *M1* structure. Without adjusting the precursor solution pH, all samples prepared to date contain the desired *M1* phase along with another phase, known as *M2*, as pseudo-hexagonal tungsten bronze-type (HTB-type) impurity. The *M1* phase cannot be crystallized from precursor solutions with pH above about 3.5. For precursor solutions with pH < 2, the product becomes highly sintered after calcination and likely does not contain the *M1* phase. The sample could not be ground into powder for XRD analysis, so the phase content has not yet been characterized. It appears that the *M1* phase is only stable within the pH range 2.8-3.5.

Chapter 1

INTRODUCTION

Ethylene, acrylic acid and acrylonitrile are becoming increasingly important in the chemical industry, and Mo-V-Nb-Te-O mixed metal oxides are the one of the most efficient catalysts for processes leading to these compounds instead of fully oxidizing to the global warming gas, carbon dioxide [1]. Nearly 1 kg of each of these chemicals is produced for every human being on Earth each year. Many chemical industries are trying to develop the commercial application of these catalysts, scaling up from laboratory scale operations.

1.1 Background Information

The orthorhombic *M1* Mo-V-O catalysts together with a promoter phase, *M2* phase, have a high activity of propane oxidation. It has much more efficiency than an amorphous Mo-V-O catalysts. Adding in some other metal elements (Te, Nb, Pd etc) will maintain this activation property, but make the synthesis condition easier to control [5]. Also, with different metal elements, the Mo-V-(M)-O catalysts express different selectivity for different alkane and alkene.

Dr. Xin Li and Prof. Douglas Buttrey have extensively discussed detailed processes for synthesis Mo-V-Nb-Te-O catalysts with the orthorhombic *M1* phase structure [2, 3]. Other chemical variations are possible with promise for other conversions; for example, SABIC has found that the mixed oxide Mo-V-Nb-Pd-O can convert readily-abundant ethane (recovered in large quantities from fracking

operations) to more valuable acetic acid. There are only a few new alkane-fed processes, leading to C2 and C3 compounds, applied in the chemical industry recent year. For example, the new propane-process AN plant built by Asahi Kasei Chemicals in Thailand in 2013 [5]. Most of other chemical conversion with these oxides remain as laboratory-scale demonstrations, and are therefore still at the development stage.

1.2 Mo-V-Nb-Te-O Mixed Metal Oxides

There are two major phases in the Mo-V-Nb-Te-O Mixed Metal Oxides: *M1* phase and *M2* phase. The Mo-V-Nb-Te-O *M1* phase catalyst is an orthorhombic structure crystal. It is a covalent framework structure comprise of pentagonal building block that are linked together with octahedra. The projection of the *M1* structure model is shown in Figure 1.2.1. Tellurium enters the structure as an intercalant primarily into hexagonal nanochannels in the framework, and also with low occupancy into heptagonal nanochannels.

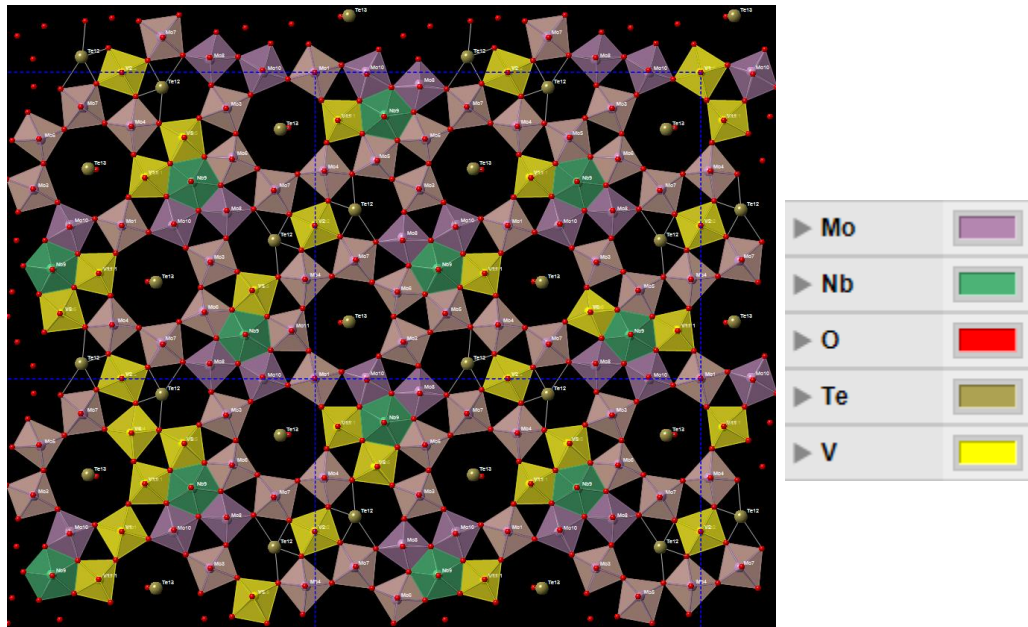


Figure 1.2.1 [001] projection of the Mo-V-Nb-Te-O *M1* structure

The *M2* phase is an orthorhombically distorted variant of a “hexagonal tungsten bronze” (HTB) structure. It is built from corner-shared octahedra and lacks the pentagonal subunits characteristic of *M1*. There are no pentagonal building blocks in *M2* phase structure, but Te also intercalates into nanochannels. The [001] view of *M2* phase is shown in Figure 1.2.2.

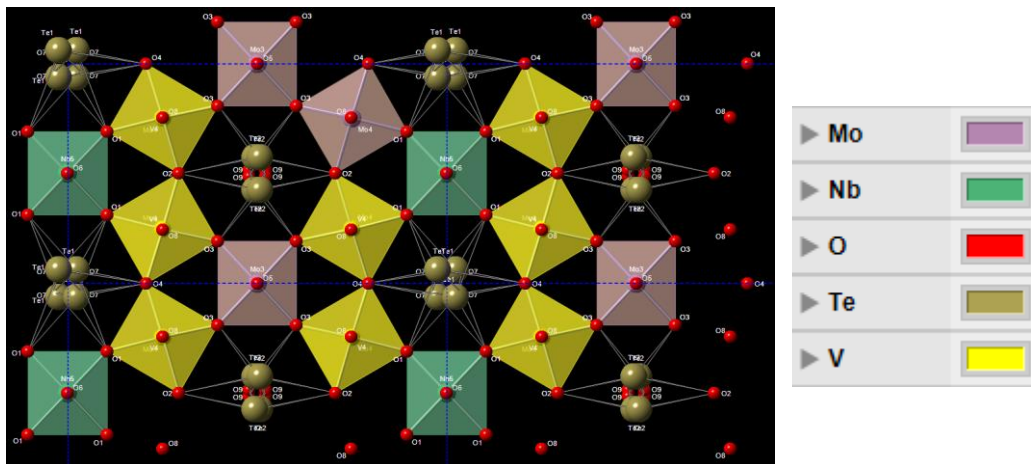


Figure 1.2.2 [001] projection of the Mo-V-Nb-Te-O *M2* structure

However, other mixed metal oxides, such as tellurium molybdate $\text{TeMo}_5\text{O}_{16}$, V-substituted Mo_5O_{14} or $(\text{V}, \text{Mo})_5\text{O}_{14}$, and Mo-substituted V_2O_5 or $(\text{Mo}, \text{V})_2\text{O}_5$, might be crystallized as impurity components while the *M1* phase crystallized, but most of my synthesized catalysts were confirmed to be the combination of *M1* and *M2* phase structure. The basic pH solution was failed to crystallize the *M1* phase.

1.3 The Selectivity of Nb, Te

Te or Nb in *M1* phase increased the selectivity of ethylene from the ethane oxidation, but adding Te or Nb into Mo-V-O *M1* phase is not necessary to active this process [3, 6]. The oxidative dehydrogenation of ethane is the second most energy consuming chemical process on the earth, as presently carried out by steam cracking in the absence of a catalyst. The *M1* phase catalyst reduced a large amount required energy of this process. The conversion of propane to acrylic acid (selective oxidation) and acrylonitrile (selective ammoxidation) requires addition of Nb or Ta and Te or Sb

into the Mo-V-O *MI* phase [3, 6]. Moreover, there are about 5.22 million tonnes acrylic acid and 6.9 million tonnes acrylonitrile produced each year [7, 8]. Increasing the selectivity and yield of the selective ammoxidation and selective oxidation of the propane could make abundant profit and expand the market size of acrylic acid and acrylonitrile.

1.4 Research Objective

In my research, I synthesized Mo-V- Nb-Te- O mixed metal oxides and studied the factors influencing the synthesis (size, shape, and contaminant) of the *MI* phase catalyst in the Mo-V- Nb-Te- O system. I tried to keep all other factors the same and change only one factor each time to analyze the influence on the size, shape and impurity of the *MI* phase catalyst. The characterization was done by comparing the X-ray diffraction (XRD) pattern from the Bruker D8 Advance Diffractometer with my calculated intensity from the Bragg's law and analyzing peak shape profiles using the Scherrer equation to estimate crystallite dimensions.

1.5 Future Path

I successfully synthesized Mo-V- Nb-Te- O orthorhombic *MI* phase catalyst, and discussed the effect of the element ratio (Mo:V:Nb:Te), argon calcination time and temperature, and pH of the mixture during my senior year. The data was analyzed by X-ray powder diffraction. Further catalyst performance will be evaluated by collaborators, Dr. Rebecca Fushimi and Dr. Anne Gaffney, at the Idaho National Laboratory using Temporal Analysis of Products (TAP), which allows for pulsing of the reactant alkane followed by time-resolve analysis of the intermediate and product species that are generated under catalyst reaction conditions. Moreover, in moving

forward, it would be helpful to apply statistical design of experiment methods to optimize the synthesis and to learn how to efficiently scale up. It would also be useful to examine ways to modify the synthesis to convert it from a batch process to a continuous operation.

Chapter 2

METHOD

The work in this thesis involves a combination of synthetic studies and characterization with X-ray powder diffraction. A more detail introduction and description of my research methods are discussed in this chapter.

2.1 Synthesis Method

There are three general approaches to the *M1* synthesis: (i) the slurry method, (ii) the hydrothermal route, and (iii) microwave-assisted hydrothermal synthesis. The slurry method is relatively easier and more commonly applied than hydrothermal route [2]. It was chosen as the focus for study in this thesis. However, the hydrothermal route has been popular for a long time too. For continuous operation, it may be best to create a hybridized approach involving continuous processing with the slurry method, but adapting it to allow for microwave heating instead of the standard resistive heating, as a created 4th method of preparation. In addition to obtaining the desired catalyst phase, it will be necessary to control the crystallite size, shape and agglomeration. Optimal characteristics will be those stable catalysts which have high activity and selectivity to the desired product in the chemical reactor. Also, reducing energy and waste carbon, and increasing the $2c/(a+b)$ ratio are required to increase the efficient of the catalysts. The impurity reduction and optimization of stoichiometry achieved by synthesis control particle geometry, which is also part of optimization. Additionally, a promoter phase, *M2*, may need to be used to enhance the reactivity, and these must be optimally blended with the active catalyst phase, which will require further engineering design strategies.

The slurry synthesis was carried out by mixing ammonium vanadate, ammonium heptamolybdate, ammonium niobium oxalate, and telluric acid in sequence, and begin the first step of crystallization during rotoevaporation at 60°C, under mild vacuum assist, to remove water until dry. Further annealing in the range 500-675°C was processed in a tube furnace with continuous argon flow though before phase evaluating by X-ray diffraction. Different phases, shapes and sizes can be obtained by adjusting various factors, such as temperature of evaporation and calcination, pH of the solution, calcination time under the air or argon gas condition, and the ratio of the metals.

2.2 Characterization Methods

This section is divided into six subsections covering X-ray Diffraction, Bragg's Law, Pseudi-Voigt approximation, Instrumental width, Scherrer equation, and calibration.

2.2.1 X-ray Diffraction

It is necessary to analyze composition, crystal structure, crystal habit (shape), and crystal size in the product Mo-V-Nb-Te-O catalyst. This involved use of X-ray powder diffraction using the ISE Lab Bruker D8 Advance Diffractometer. Compositional analysis will require use of scanning electron microscopy together with energy dispersive X-ray microanalysis. For commercialization, methods of rapid identification/verification of the catalyst phases in operando will be required, so methods of “fingerprint” peak identification by X-ray diffraction need to be developed. Rapid characterization would presumably involve both analysis of the phase content and assessment of the crystallite morphology to maintain consistency.

However, in my research, it only involved X-ray diffraction by using Bruker D8 Advance Diffractometer. The XRPD data were exported in the form of xy files (i.e. 2θ , intensity pairs) for use with several software packages, CrystalDiffract, Rietica, and Excel.

The intensity of X-ray diffraction also can be calculated for a given Miller indices hkl , which will occur at the peak center 2θ position consistent with Bragg's Law (discussed in chapter 2.2.2). The X-ray diffraction pattern can also be obtained from CrystalDiffract by plug in the atomic coordinates and the symmetry from the literatures. Figure 2.2.1.1 is the X-ray diffraction pattern from the CrystalDiffract for Mo-V-Nb-Te-O $M1$ phase ($0^\circ < 2\theta < 80^\circ$; the X-ray diffraction pattern for the whole range is in Appendix A), and the related atomic coordinates are listed in Table 2.2.1.1. The XRD pattern and atomic coordinates of $M2$ phase are shown in Figure 2.2.1.2 and Table 2.2.1.2, respectively. The atomic coordinates and XRD patterns for other possible structures in my research, such as tellurium molybdate $\text{TeMo}_5\text{O}_{16}$, V-substituted Mo_5O_{14} or $(\text{V}, \text{Mo})_5\text{O}_{14}$, and Mo-substituted V_2O_5 or $(\text{Mo}, \text{V})_2\text{O}_5$, were obtained by the same way. However, there is no intense peaks for these structures in my research samples that crystallized $M1$ phase structure successfully.

Table 2.2.1.1 Atomic coordinates and occupancies for all sites in the Mo-V-Nb-Te-O
M1 phase; space group *Pba2* (no.32); a=21.134(1) Å, b=26.647(1) Å,
c=4.0140(2) Å: Z=4³

Atom type	Atom #	Site	x	y	z	Occupancy
Mo	1a	Mo1	0	0	0.5	0.699(31)
V	1b	V1	0	0	0.5	0.301(31)
Mo	2a	Mo2	0	0.5	0.620(9)	0.421(27)
V	2b	V2	0	0.5	0.620(9)	0.579(27)
Mo	3a	Mo3	0.1175(7)	0.2284(6)	0.466(7)	0.573(20)
V	3b	V3	0.1175(7)	0.2284(6)	0.466(7)	0.427(20)
Mo	4a	Mo4	0.1767(6)	0.4774(5)	0.513(7)	0.804(22)
V	4b	V4	0.1767(6)	0.4774(5)	0.513(7)	0.196(22)
Mo	5a	Mo5	0.2119(6)	0.3427(4)	0.627(7)	0.954(20)
V	5b	V5	0.2119(6)	0.3427(4)	0.627(7)	0.046(20)
Mo	6a	Mo6	0.2800(5)	0.2118(4)	0.646(7)	0.883(21)
V	6a	V6	0.2800(5)	0.2118(4)	0.646(7)	0.117(21)
Mo	7a	Mo7	0.3841(6)	0.1018(5)	0.491(7)	0.760(20)
V	7b	V7	0.3841(6)	0.1018(5)	0.491(7)	0.240(20)
Mo	8	Mo8	0.4594(5)	0.2278(4)	0.635(7)	1
Nb	9	Nb9	0.3591(5)	0.3177(4)	0.493(6)	1
Mo	10	Mo10	0.0014(6)	0.1329	0.660(6)	1
Mo	11a	Mo11	0.3427(5)	0.4409	0.642(6)	0.948(25)
V	11b	V11	0.3427(5)	0.4409	0.642(6)	0.052(25)
Te	12	Te12	0.5498(7)	0.1042	0.544(8)	0.711(10)
Te	13	Te13	0.6852(32)	0.4118	0.317(17)	0.146(7)
O	14	O1	0	0	0.018(9)	1
O	15	O2	0	0.5	0.061(10)	1
O	16	O3	0.1192(8)	0.2297(6)	0.032(7)	1
O	17	O4	0.1767(7)	0.4748(5)	0.063(8)	1
O	18	O5	0.2123(7)	0.3385(5)	0.026(8)	1
O	19	O6	0.2830(7)	0.2146(5)	0.085(8)	1
O	20	O7	0.3866(7)	0.1062(5)	0.061(8)	1
O	21	O8	0.4520(7)	0.2279(7)	0.021(7)	1
O	22	O9	0.3561(7)	0.3199(6)	0.058(8)	1
O	23	O10	0.9944(7)	0.1355(5)	0.084(7)	1
O	24	O11	0.3439(7)	0.4398(6)	0.052(9)	1
O	25	O12	0.5506(11)	0.1122(7)	0.022(8)	0.711(10)
O	26	O13	0.5224(7)	0.4300(5)	0.550(9)	1
O	27	O14	0.5743(7)	0.3340(5)	0.553(9)	1

O	28	O15	0.0425(7)	0.2692(5)	0.581(8)	1
O	29	O16	0.5801(8)	0.0354(7)	0.564(9)	1
O	30	O17	0.7015(9)	0.2958(7)	0.630(7)	1
O	31	O18	0.7760(7)	0.2149(5)	0.562(8)	1
O	32	O19	0.6677(7)	0.0956(5)	0.568(9)	1
O	33	O20	0.9631(8)	0.4335(7)	0.574(10)	1
O	34	O21	0.8147(6)	0.3514(6)	0.582(7)	1
O	35	O22	0.7984(6)	0.1243(5)	0.542(8)	1
O	36	O23	0.7700(6)	0.0302(6)	0.576(8)	1
O	37	O24	0.8687(7)	0.2559(5)	0.545(9)	1
O	38	O25	0.9065(6)	0.1150(6)	0.565(8)	1
O	39	O26	0.9087(7)	0.0164(6)	0.531(7)	1
O	40	O27	0.8334(8)	0.4552(6)	0.603(7)	1
O	41	O28	0.9457(7)	0.3411(6)	0.565(8)	1
O	42	O29	0.9511(7)	0.1986(6)	0.568(9)	1
O	43	O30	0.1508(7)	0.2995(6)	0.543(8)	1
O	44	O31	0.682(5)	0.433(4)	0.975(27)	0.146(7)

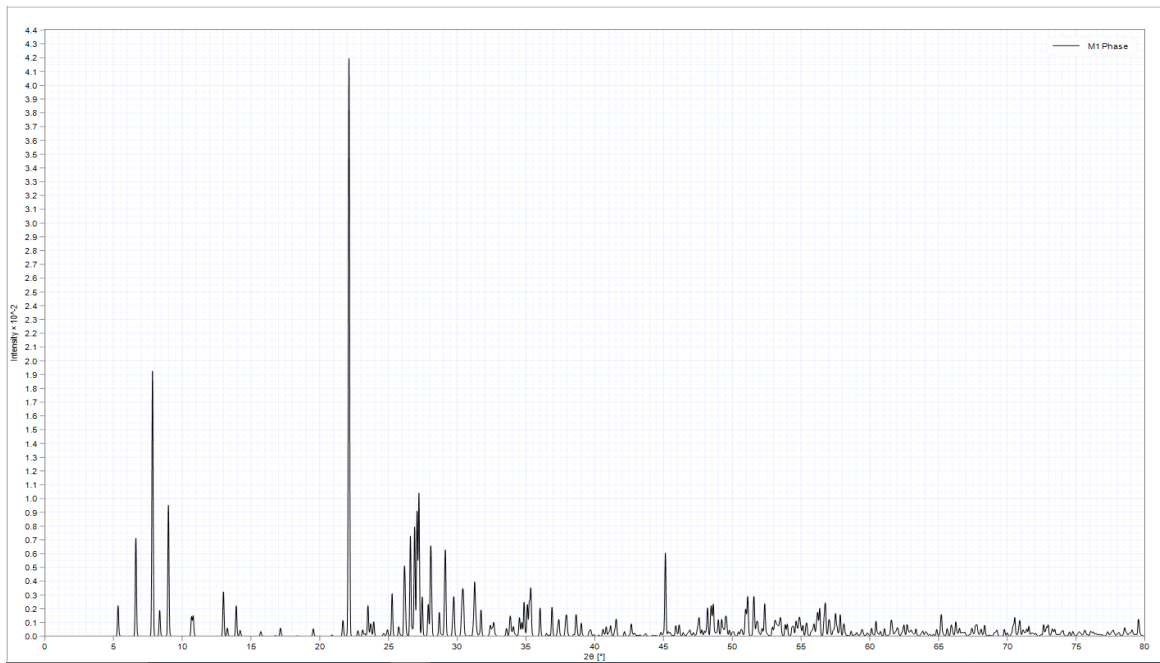


Figure 2.2.1.1 The X-ray diffraction pattern simulated from CrystalDiffract (software) for Mo-V-Nb-Te-O *MI* phase ($0^\circ < 2\theta < 80^\circ$)

Table 2.2.1.2 Atomic coordinates and occupancies for all sites in the Mo-V-Nb-Te-O *M2* phase; space group *Pmm2* (no.25); a=12.6294(6) Å, b=7.2956(30) Å, c=4.02010(7) Å: Z=4⁹

Atom type	Atom #	Site	x	y	z	Occupancy
Te	4i	Te1	0.0237(26)	0.0621(18)	0.609(5)	0.237(5)
Te	4i	Te2	0.507(39)	0.5754(19)	0.624(5)	0.218(4)
Mo	1c	Mo3	0.5	0	0.577(14)	0.54(4)
V	1c	V3	0.5	0	0.577(14)	0.46(4)
Mo	4i	Mo4	0.2505(8)	0.2463(11)	0.583(6)	0.78(1)
V	4i	V4	0.2505(8)	0.2463(11)	0.583(6)	0.22(1)
Mo	1b	Mo5	0	0.5	0.594(9)	0.5
Nb	1b	Nb5	0	0.5	0.594(9)	0.5
O	4i	O1	0.1047(10)	0.3098(12)	0.589(4)	1
O	2f	O2	0.2935(13)	0.5	0.583(5)	1
O	4i	O3	0.3965(10)	0.1913(12)	0.596(4)	1
O	2e	O4	0.7933(13)	0	0.565(5)	1
O	1c	O5	0.5	0	0.086(6)	1
O	1b	O6	0	0.5	0.065(6)	1
O	4i	O7	0.0387(18)	0.0425(36)	0.103(7)	0.237(5)
O	4i	O8	0.2514(13)	0.2445(18)	0.076(4)	1
O	4i	O9	0.4778(19)	0.4855(54)	-0.004(10)	0.218(4)

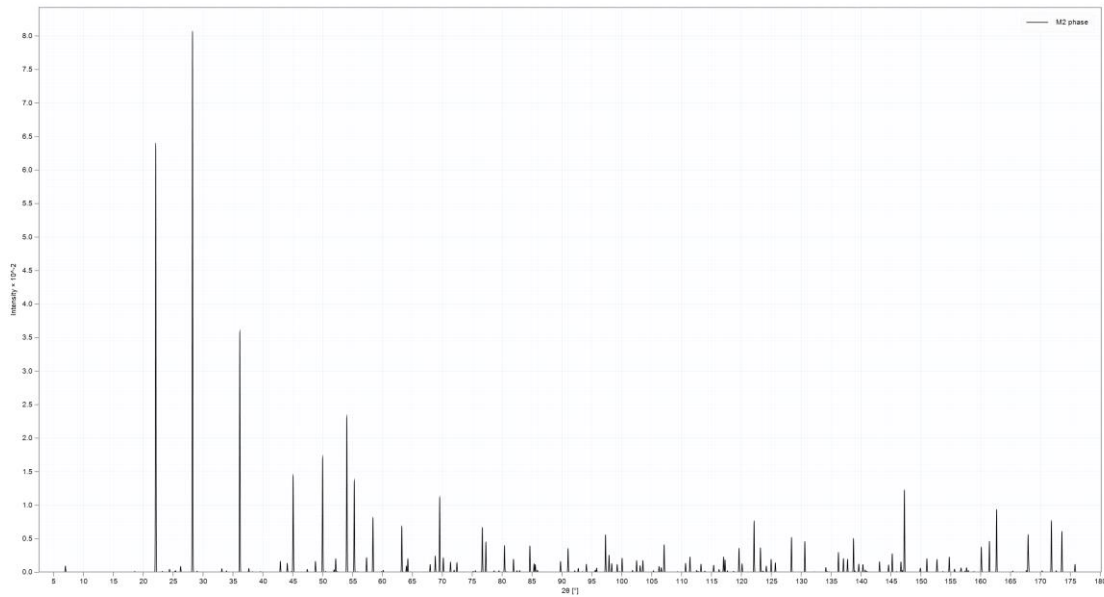


Figure 2.2.1.2 The simulated X-ray diffraction pattern from CrystalDiffract for Mo-V-Nb-Te-O *M2* phase

2.2.2 Bragg's Law

Bragg's law associates the scattering angles from a crystal lattice with d – spacings for conditions under which constructive interference occurs in diffraction experiments at a particular wavelength, λ . The equation is written as:

$$n \cdot \lambda = 2d \sin \theta$$

λ is 0.15406 nm for the incident X-ray beam used in all experiments in this thesis. n is the order of interference. In my intensity calculation, Only 1st-order diffraction was considered, since the higher-order diffraction folds into the $n = 1$ analysis with spacings of d/n . d is the spacing between Miller planes in crystal structure, which depends on Miller indices (hkl) and crystal geometry. θ is the scattering angle. 2θ should in the range of $0^\circ < 2\theta < 180^\circ$; however, it is often sufficient to collect data only out to about 2θ of about 60-80° maximum. The minimum angle is

chosen based on the lowest expected peak position for the pattern to be collected and allowing for some variations in instrument calibration. Figure 2.2.2.1 is a schematic to explain how constructive and destructive interference lead to intensity only at positions satisfying Bragg's law.

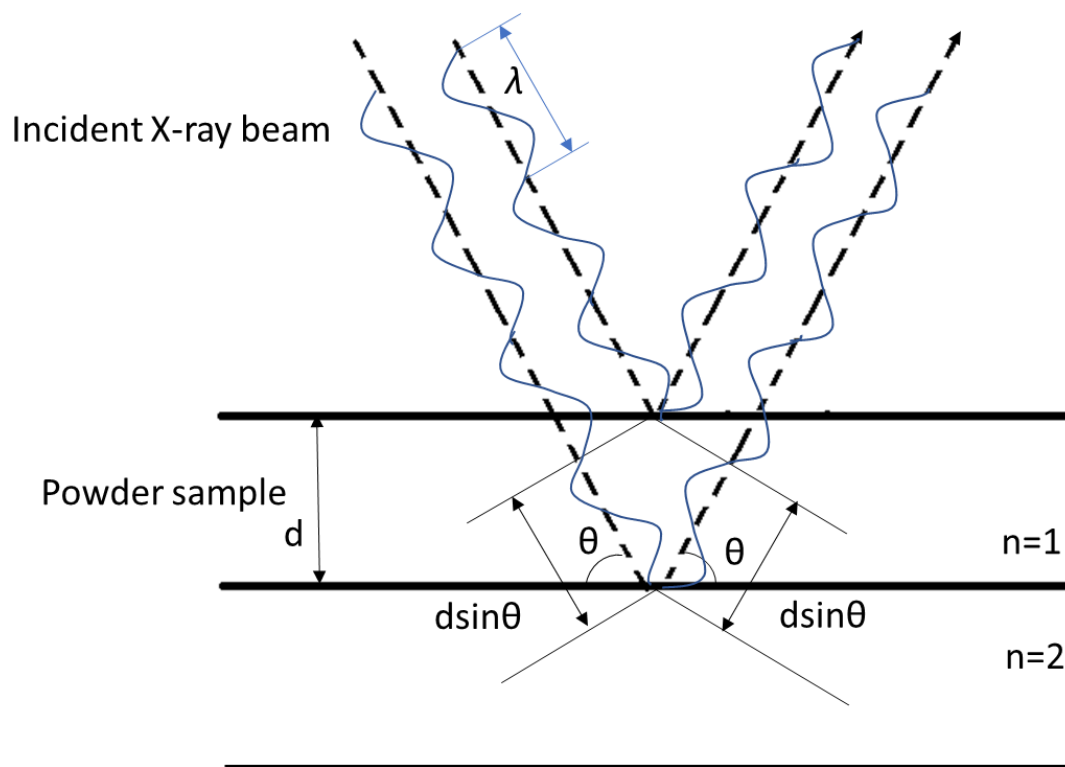


Figure 2.2.2.1 The interpretation of Bragg's law

2.2.3 Pseudo-Voigt approximation

The peaks of intensity in XRD patterns given by any x-ray diffractometer, including the Bruker D8 Advance Diffractometer. X-ray diffraction produces a peak profile that is a convolution of Normal (Gaussian) and Cauchy (Lorentzian) probability

distribution functions (PDFs). The convolution of these two functions is very cumbersome, and is known as the Voigt convolution. The pseudo-Voigt function is an approximation to the true convolution that is more mathematically tractable for routine calculations. It is a linear combination of Gaussian distribution and Lorentzian curves. The peak shapes from the pseudo-Voigt approximation, Gaussian distribution and Lorentzian distribution are shown in Figure 2.2.3.1. The Matlab code for the addition of pseudo-Voigt curves is attached in Appendix B.

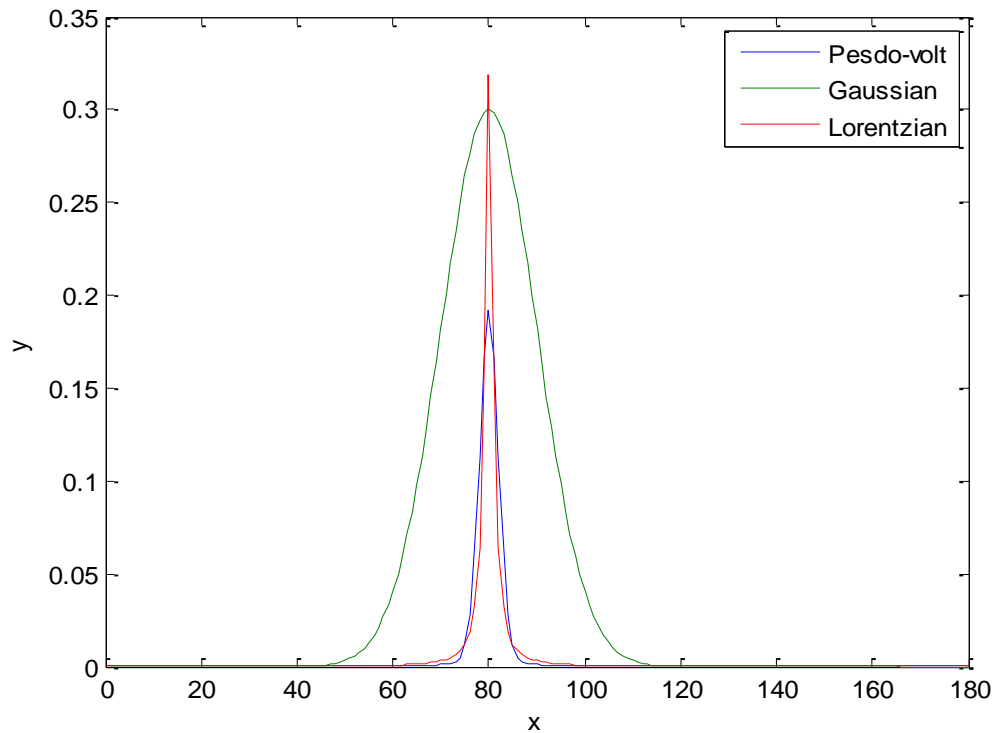


Figure 2.2.3.1 The comparison on the peak shapes from the pseudo-Voigt approximation, Gaussian distribution and Lorentzian distribution.

The overlapping of two peaks distributes similar to the large and wide one. If the specimen has smaller crystallite dimensions such that the peak shape profile is broadened, then the result is again a convolution of the instrument and the specimen contributions. If the specimen contribution is sufficiently broadened, then there may be no need to consider the minor contribution from the influence of the instrument resolution (See Figure 2.2.3.2). However, as the peak narrows to down, the influence of the instrumental width becomes greater; therefore, the shape of the broad peak is more closely to the peak of the sample in Bruker D8 XRD.

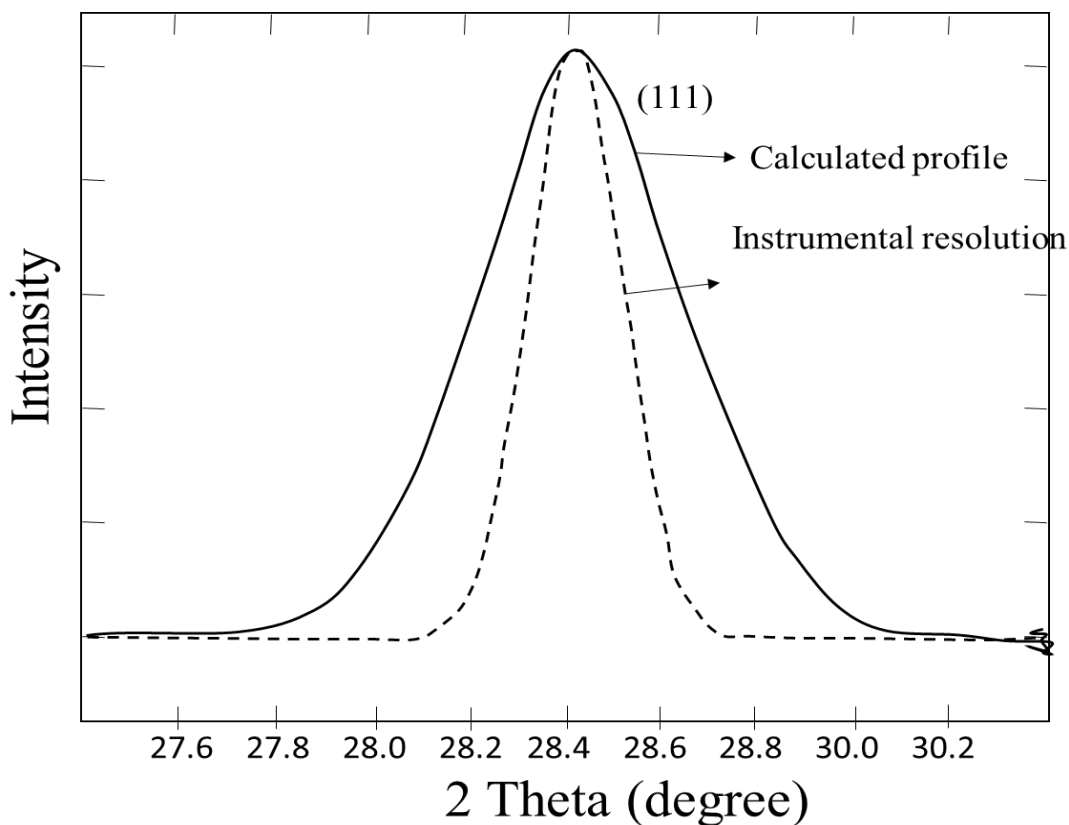


Figure 2.2.3.2 The measurement of the Bruker D8 Advance Diffractometer instrumental width

When the sample highly crystallized and the peak width of the sample is smaller than instrumental width, the apparent peak broadening only represents the instrumental resolution, and does not reveal evidence of specimen crystallite geometry. Therefore, from Scherrer equation (Chapter 2.25), only if the full width at half maximum (FWHM) of my synthesized catalyst is larger than the instrumental width, the peaks in that XRD pattern can be used for crystal size and shape analysis. The Si standard has large enough crystallites to provide an instrument-resolution-limited profile. It was one of the standard sample to measure the instrument width of the Bruker D8 XRD in ISE lab. Detailed peak profile measurements and the Scherrer calculations of crystallite dimensions were discussed in next two sessions.

2.2.4 Instrumental Width

To identify the phase structure of Mo-V- Nb-Te- O catalyst, we only interested in the intensity of the catalyst over the range of $0^\circ < 2\theta < 55^\circ$. Making sure that the instrumental width was smaller than the full width at half maximum of my sample under 55° Bragg's angle was needed. Since silicon is one of the common standard sample to indicate the instrument (discussed in chapter 2.2.3), obtaining the FWHM of the silicon standard X-ray diffraction pattern was an important step before characterizing the structure of Mo-V- Nb-Te- O catalyst.

Table 2.2.4.1 shows the characteristic peak of the silicon standard sample for the Bruker D8 XRD in ISE lab. However, since a more accurate and smooth curve on the peak width vs 2θ graph were required to determine the acceptable FWHM at each angle, we extended the angle range to 80° .

Table 2.2.4.1 Miller indexes and scattering angles for NIST Silicon Standard Reference Material (SRM 640e) at 22.5°C using Cu $K_{\alpha 1}$ radiation with $\lambda = 0.15405929$ nm and using lattice parameter $a = 0.35713526$ nm¹⁰.

<i>h</i>	<i>k</i>	<i>l</i>	2θ
1	1	1	28.441
2	2	0	47.300
3	1	1	56.120
4	0	0	69.126
3	3	1	76.372
4	2	2	88.025
5	1	1	94.947
4	4	0	106.701
5	3	1	114.084
6	2	0	127.534
5	3	3	136.880

The data of intensity for the silicon standard sample were collected from the Bruker D8 XRD in ISE lab and plotted in excel. Figure 2.2.4.1 was the overall intensity trends for the silicon standard sample, and the FWHM measurement of the highest intensity peak ($hkl=111$) was shown in Figure 2.2.4.2, the zoom in intensity plot as an example.

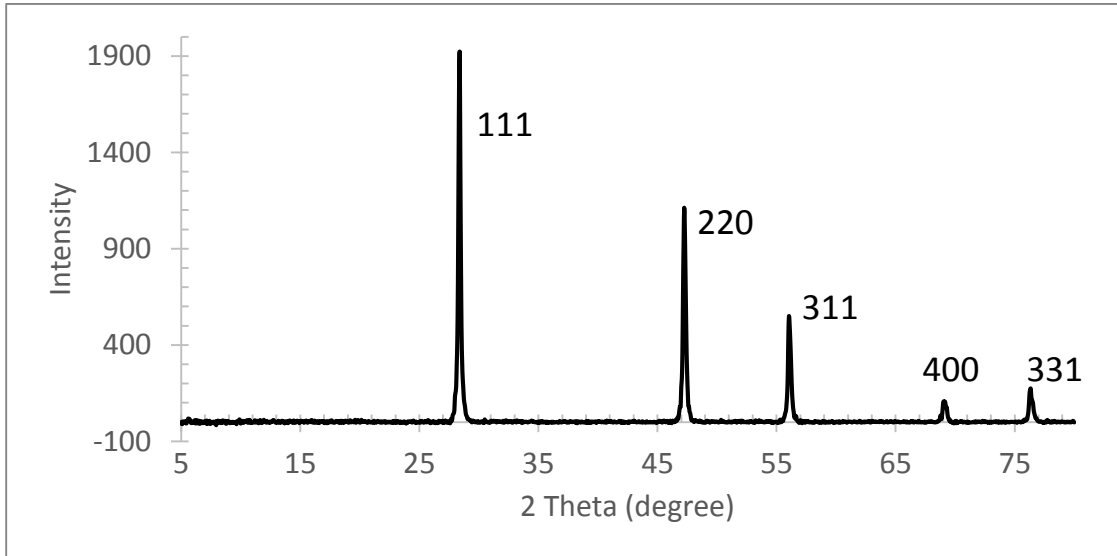


Figure 2.2.4.1 The expected X-ray diffraction profile from the NIST Si Standard SRM 640e ($5^\circ < 2\theta < 80^\circ$) (hkl on figures) using a Cu $K\alpha$ source.

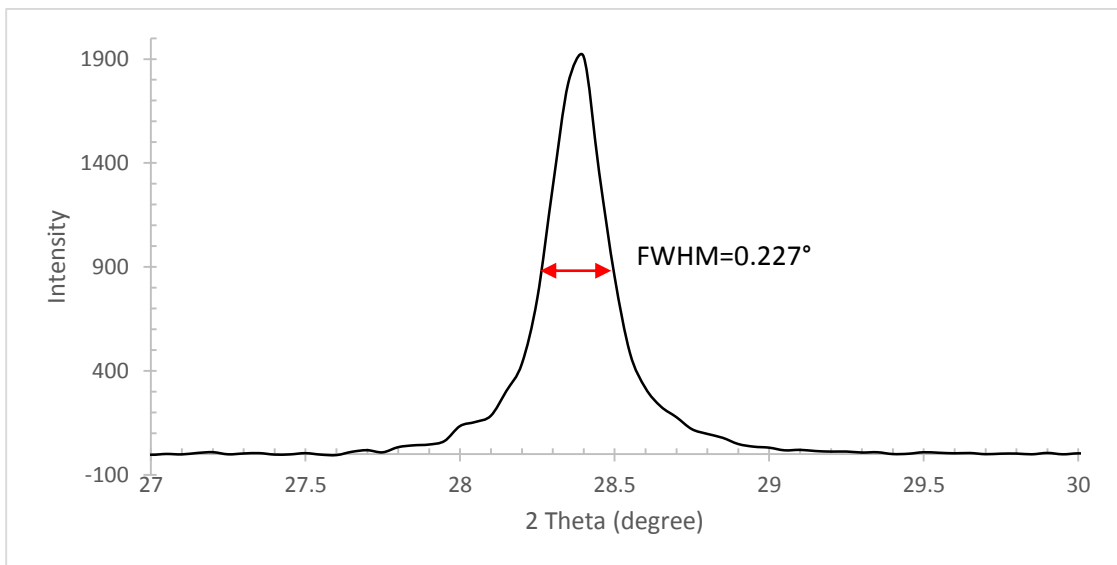


Figure 2.2.4.2 The (111) peak intensity from the NIST Si Standard SRM 640e showing an instrument-limited full width at half maximum of $0.227(2)^\circ$. This peak should be centered at 28.441° and can be used, along with other standard peak positions, to determine the systematic zero point correction for the instrument. Analysis must also account for the presence of a shoulder peak at 28.513° corresponding to the $K\alpha_2$ contribution, which has intensity that is half that of $K\alpha_1$

The rest of zoom in plots for other characteristic peaks of the standard silicon are attached in Appendix C. All the FWHM, same as the instrumental width, were tabled in Table 2.2.4.2. The instrumental width vs 2 theta curve is shown in Figure 2.2.4.3. The width on the curve indicates the instrumental width contributed by the Bruker D8 as it is configured with a Vario monochromater and 1.2 mm slit configuration. Any samples with the FWHM above this curve can be measured, and the samples FWHM smaller these widths will measure the instrumental width instead. The measurable crystal size can be calculated from FWHM by Scherrer equation, which discussed in chapter 2.2.5. In our case, the Mo-V- Nb-Te- O catalyst with the crystal size about or below 300 Å can be measured from the Bruker D8 XRD in ISE lab.

Table 2.2.4.2 The instrumental width and crystal size (The width is indicated by the FWHM of intensity peaks of the silicon standard sample. The unit is in rad. The crystal size is calculated from Scherrer equation)

<i>h</i>	<i>k</i>	<i>l</i>	2θ	$\cos(\theta)$	FWHM (degree)	Width (rad)	$t(\text{Å})$
1	1	1	28.441	0.9694	0.2269	0.00396	361.27
2	2	0	47.300	0.9160	0.2730	0.00476	317.74
3	1	1	56.120	0.8825	0.2848	0.00497	316.04
4	0	0	69.126	0.8235	0.3423	0.00598	281.79
3	3	1	76.372	0.7860	0.3036	0.00530	332.87

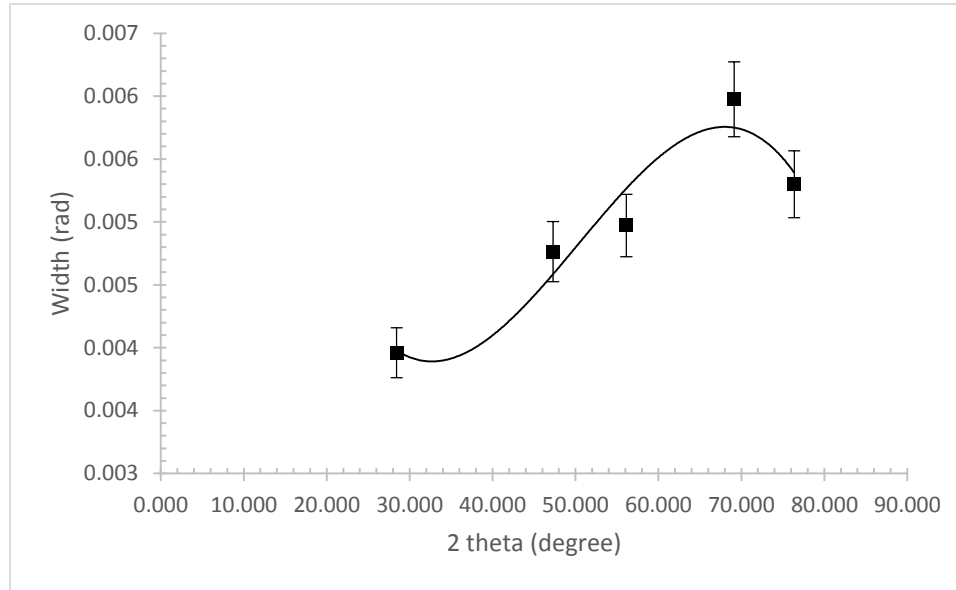


Figure 2.2.4.3 The instrumental width for Bruker D8 XRD in ISE lab.

2.2.5 Scherrer Equation

The Scherrer equation is an equation to calculate the crystal size. It can be used to determine the crystal shape together with X-ray diffraction pattern. The Miller indices (hkl) indicate the dimension of the crystal and Scherrer equation can measure the size of crystal normal to the (hkl) planes. The equation is written as:

$$t = \frac{K * \lambda}{\beta * \cos\theta}$$

The wavelength, λ , is 0.15406 nm. β is the FWHM in radians. t is the dimension perpendicular to the hkl of the peak being measured, and the unit of it is the same as the wavelength λ . The shape factor K depends on the geometry of the crystals. It is typically assumed to be approximately 0.9 when the shape is unknown. The sizes of silicon standard sample on different dimensions were listed in Table. 2.2.4.2 in

Chapter 2.2.4, and the sizes of the Mo-V- Nb-Te- O *MI* phase catalyst were discussed in Chapter 5.

2.2.6 Calibration

To calibrate the X-ray Diffraction data from the Bruker D8 XRD, I used the peak position associated with the (001) planes. This peak is strong with a *d*-spacing very close to 4.0 Å for all of the molybdenum bronze phases, representing the unique axis for stacking of the octahedra. *M1* and *M2* have this peak at 2θ center positions with only a very slight separation, such that they are strongly overlapped. If either *M1* or *M2* dominates in the specimen, then the (001) position can be assigned to the dominant phase peak as a reference. In my research, the *M1* phase (001) position was used as a reference position, which the Bragg's angle (2θ) was calculated to be 22.127°; therefore, all the X-ray Diffraction patterns were shift to specific angles to match (001) peak with 22.127° angle position.

Chapter 3

PRECALCULATION

XRPD intensity calculations were carried out in addition to using CrystalDiffract software for confirming the location and intensity of individual peaks in the complex diffraction patterns from *M1* and *M2* preparations. For my research, determining the reagents weight and analyzing the XRD pattern of *M1* and *M2* phase Mo-V-Nb-Te-O catalyst from the coordination given by Peter DeSanto Je, Douglas J. Buttrey, and Robert K. Grasselli are two of important calculation before synthesis Mo-V-Nb-Te-O catalyst [9].

3.1 Determining Mass Proportions of Reagents

The mass proportions of reagents were determined by the metal ratio. The ranges of the metal ratio are as high as Mo:V:Nb:Te = 1:0.33:0.11:0.22 in Xin Li's experiment, and as low as Mo:V:Nb:Te = 1:0.2:0.13:0.11 in Dr. Johan Holmberg's article [2, 11]. We decided to use the ratio Mo:V=1:0.31, 1:0.24, and 1:0.22.

The text is dealing with the metal ratios measured with respect to the dominant metal, molybdenum. The mole ratios are set up as 1:x:y:z for Mo:V:Nb:Te. This is one common way of representing the composition. An alternative way is to recognize that the framework, without the intercalated species, can be represented as Mo₁₀O₂₈. The framework metal ratios (sans intercalated Te or Sb) can then be expressed with values that sum to 10 for Mo, V, and Nb, and also have the appropriate ratios consistent with the representation presented earlier. The generic formula can be expressed as {TeO}_x•(Mo,V,Nb)₁₀O₂₈. x is a number between 0 and 1. According to the bond valence of each set element in *M1* phase (listed in Table 3.1.1), x can be calculated by making the crystal neutral.

Table 3.1.1 The bond valence of each set element in *MI* phase.

Atom type	Atom #	Atom Site	x	y	z	Occupancy	Mo valence	V valence	Nb valence	Te valence
Mo	1a	Mo1	0	0	0.5	0.699	5			
V	1b	V1	0	0	0.5	0.301		4		
Mo	2a	Mo2	0	0.5	0.620	0.421	5			
V	2b	V2	0	0.5	0.620	0.579		4		
Mo	3a	Mo3	0.1175	0.2284	0.466	0.573	5			
V	3b	V3	0.1175	0.2284	0.466	0.427		5		
Mo	4a	Mo4	0.1767	0.4774	0.513	0.804	5			
V	4b	V4	0.1767	0.4774	0.513	0.196		5		
Mo	5a	Mo5	0.2119	0.3427	0.627	0.954	6			
V	5b	V5	0.2119	0.3427	0.627	0.046		5		
Mo	6a	Mo6	0.2800	0.2118	0.646	0.883	6			
V	6a	V6	0.2800	0.2118	0.646	0.117		5		
Mo	7a	Mo7	0.3841	0.1018	0.491	0.76	5			
V	7b	V7	0.3841	0.1018	0.491	0.24		5		
Mo	8	Mo8	0.4594	0.2278	0.635	1	6			
Nb	9	Nb9	0.3591	0.3177	0.493	1			5	
Mo	10	Mo10	0.0014	0.1329	0.660	1	6			
Mo	11a	Mo11	0.3427	0.4409	0.642	0.948	6			
V	11b	V11	0.3427	0.4409	0.642	0.052		5		
Te	12	Te12	0.5498	0.1042	0.544	0.711				4
Te	13	Te13	0.6852	0.4118	0.317	0.146				4

Then, the metal ratio can be found, and the mass proportions of reagents can be calculated from the formula weight of each reagent and the molar number of the metal in 1 mole reagent based on the ratio we found. They are Mo:V:Nb:Te = 1:0.31:0.14:0.27, Mo:V:Nb:Te = 1:0.24:0.13:0.12, and Mo:V:Nb:Te = 1:0.22:0.12:0.26. Tellurium is very easy to volatilize under high temperature during calcination. So, the ratio of Te to Mo was set to be 1:0.27 for all three sample. Since V is the lightest reagent, it needs to be weight first and recalculated the ratio of other reagent follow the above calculation again before weighting them.

3.2 Intensity Calculation

The intensities at different Bragg's angles, calculated from different hkl index, are by the structure factors, and corrected by the multiplicity, Lorentz-Polarization factor, and thermal factor. The equation is:

$$I_{\{hkl\}} = (F_{hkl} \cdot F_{hkl}^*) P \left[\frac{1 + \cos^2(2\theta)}{\sin^2(\theta) \cos(\theta)} \right] \exp\left(-\frac{B \sin^2(\theta)}{\lambda^2}\right)$$

F_{hkl} is the structure factor, and F_{hkl}^* is the complex conjugate of the structure factor. $F_{hkl} = \sum_{i=1}^N f_i \exp[2\pi i(hx_i + ky_i + lz_i)]$. f_i is atomic scattering factors, and it is estimated by Cromer-Mann coefficients, a set of 9 coefficients for different element. P is the multiplicity. It is different for different crystal structures and different hkl index. The determination of multiplicity is shown in Table 3.2.1.

Table 3.2.1 The multiplicity for powder diffraction data

Cubic	<i>hkl</i>	<i>hhl</i>	<i>0kl</i>	<i>0kk</i>	<i>hhh</i>	<i>00l</i>	
	48	24	24	12	8	6	
Tetragonal	<i>hkl</i>	<i>hhl</i>	<i>0kl</i>	<i>hk0</i>	<i>hh0</i>	<i>0k0</i>	<i>00l</i>
	16	8	8	8	4	4	2
Orthorhombic	<i>hkl</i>	<i>0kl</i>	<i>h0l</i>	<i>hk0</i>	<i>h00</i>	<i>0k0</i>	<i>00l</i>
	8	4	4	4	2	2	2
Hexagonal & Rhombohedral	<i>hk•l</i>	<i>hh•l</i>	<i>0k•l</i>	<i>hk•0</i>	<i>hh•0</i>	<i>0k•0</i>	<i>00•l</i>
	24	12	12	12	6	6	2
Monoclinic	<i>hkl</i>	<i>h0l</i>	<i>0k0</i>				
	4	2	2				
Triclinic	<i>hkl</i>						
	2						

$\frac{1+\cos^2(2\theta)}{\sin^2(\theta)\cos(\theta)}$ is Lorentz-Polarization factor, and $\exp\left(-\frac{B\sin^2(\theta)}{\lambda^2}\right)$ is the thermal factor. Since thermal factor has less effect and is difficult to estimate, there is no thermal factor in my intensity calculation. The calculated intensity of Mo-V-Nb-Te-O *M1* phase and *M2* phase are plotted in Figure 3.2.1 and Figure 3.2.2 respectively.

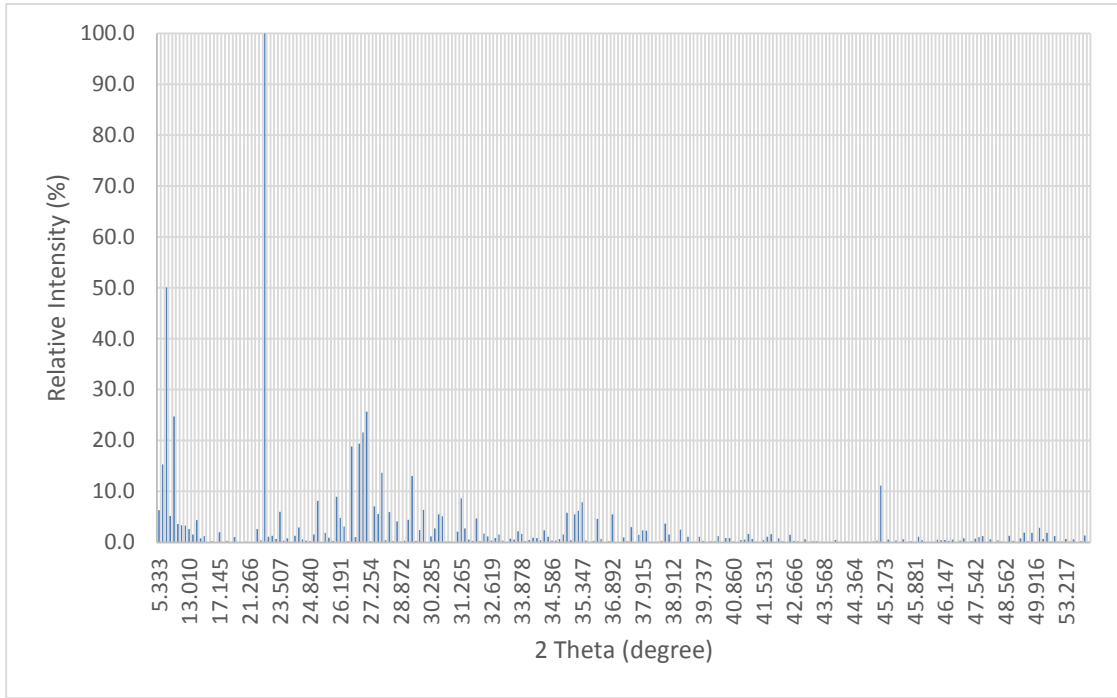


Figure 3.2.1 The calculated relative intensity of Mo-V-Nb-Te-O *MI* phase in the Bragg angle range $5^\circ < 2\theta < 55^\circ$ without peak profiles.

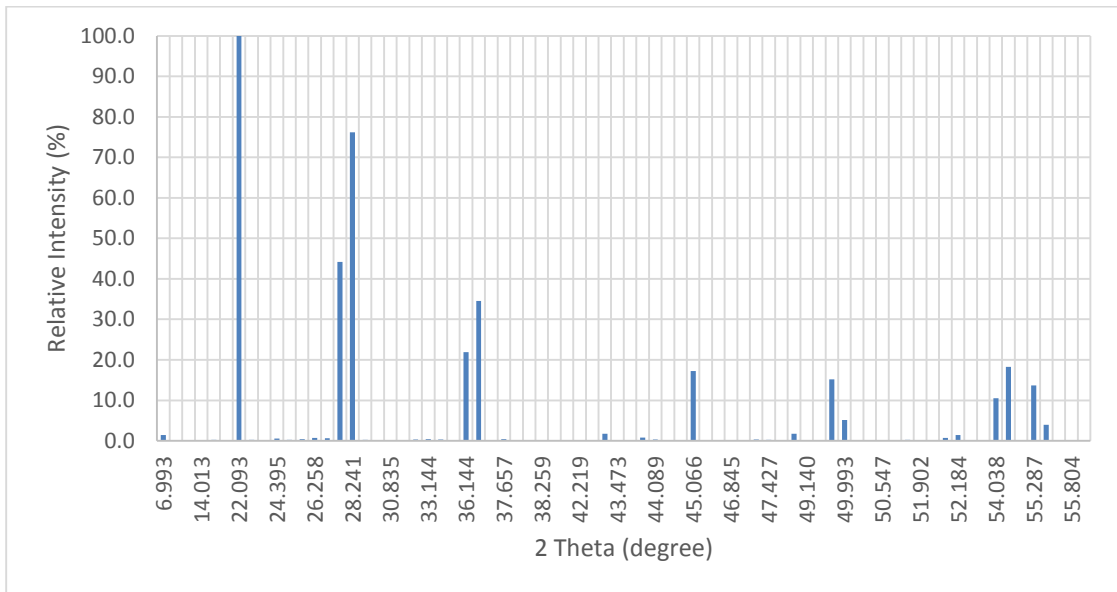


Figure 3.2.2 The calculated relative intensity of Mo-V-Nb-Te-O *MI* phase in the Bragg angle range $5^\circ < 2\theta < 55^\circ$ without peak profiles.

Chapter 4

SYNTHESIS OF Mo-V-Nb-Te-O

4.1 Introduction

The *MI* phase was synthesized by mixing ammonium vanadate NH_4VO_3 , ammonium heptamolybdate tetrahydrate $(\text{NH}_4)_6\text{Mo}_7\text{O}_{24}\cdot 4\text{H}_2\text{O}$, telluric acid H_6TeO_6 , and ammonium niobium oxalate $\text{NH}_4[\text{NbO}(\text{C}_2\text{O}_4)_2(\text{H}_2\text{O})_2]\cdot 8\text{H}_2\text{O}$ in sequence. Evaporation and furnace calcination were applied afterward. The catalyst structure and phase were evaluated by X-ray diffraction.

4.2 Experimental

The ammonium vanadate, ammonium heptamolybdate tetrahydrate, telluric acid, and ammonium niobium oxalate were weighted as calculated before and dissolved in 10 ml. The ammonium vanadate, ammonium heptamolybdate tetrahydrate, and telluric acid were heated and stirred on hot plates, but ammonium niobium oxalate was stirred without heating. After the temperature of three solutions (containing Mo, V, Te) reached 80°C , ammonium vanadate (yellow solution) was added into ammonium heptamolybdate tetrahydrate solution (clear, transparent). The color of the mixture was still light yellow. After adding telluric acid (clear, transparent) into the mixture, the new mixture turned into red. The resulting mixture was cooled to room temperature and ammonium niobium oxalate was subsequently added. The final mixture changed from red to transparent orange. After stirring for 30 mins, the solution was left to digest overnight prior to evaporation.

The first step of self-assembly began before rotoevaporation at 60°C with low pressure to remove water until dry. The clear orange solution turned into turbid orange liquid. Further calcination under air and argon condition was needed in a tube furnace.

The characterization was carried out using X-ray powder diffraction (XRPD). All the powder samples were heated in air for 2h under 275°C. Before argon calcination under about 500-675°C, 100 ml/min argon gas was flowing into the furnace for 1h. Wait until there was no air in the furnace increase the temperature slowly to about 500-675°C, and calcined the sample under this condition for 2h. In order to study the influence of the calcination time on the product characteristics, as series of calcination times longer than 2 hours were used. Argon gas flow was continued throughout the furnace cooling down to 100°C to avoid drawing oil from the bubbler back into the annealing system. Afterward, the black powder product was not removed from the furnace until the next day, when XRD analysis was performed.

The component metals ratio of each analysis was listed in Table 4.2.1, and the detail conditions of each experiment for different factor studies were shown in Table 4.2.2, Table 4.2.3 and Table 4.2.4.

Table 4.2.1 The ratio of the component metals in the mixture

x	Ratios							
	Medium V/Mo ratio	High V/Mo ratio	Low V/Mo ratio	Argon calcination time	Argon calcination temperature (boundary)	Acidic Condition	Basic Condition	pH boundary
Mo	1	1	1	1	1	1	1	1
V	0.24	0.31	0.22	0.22	0.22	0.22	0.20	0.22
Nb	0.13	0.14	0.12	0.12	0.12	0.11	0.11	0.12
Te	0.27	0.27	0.26	0.26	0.27	0.26	0.26	0.26

Table 4.2.2 The calcination condition set up to analyze the effect of ratio, and argon calcination temperature

Sample#	Medium V/Mo ratio			High V/Mo ratio			Low V/Mo ratio		
	1	2	3	1	2	3	1	2	3
Calcination temperature(°C)	575	600	625	575	600	625	575	600	625
Calcination time Air (h)	2	2	2	2	2	2	2	2	2
Calcination time Ar (h)	2	2	2	2	2	2	2	2	2

Table 4.2.3 The calcination condition set up to analyze the effect of argon calcination temperature and time

Sample#	Argon calcination time			Argon calcination temperature (boundary)							
	1	2	3	1		2		3			
Calcination temperature (°C)	625	625	625	500		550		675			
Calcination time Air (h)	2	2	2	2		2		2			
Calcination time Ar(h)	2	4	6	2	12	24	48	72	96	2	2

Table 4.2.4 The condition set up for the pH analysis

Sample#	Higher pH			Lower pH			pH limit (boundary)		
	1	2	3	1	2	3	1	2	3
pH	3.23	1.97	1.27	3.32	4.47	9.26	3.52	3.35	3.23
Calcination temperature (°C)	600	600	600	600	600	600	600	600	600
Heating time Air (h)	2	2	2	2	2	2	2	2	2
Calcination time Ar (h)	2	2	2	2	2	2	2	2	2

Chapter 5

DETERMINATION OF FACTORS INFLUENCING HABIT

5.1 Metal Ratio

The metal ratios were determined to be Mo:V:Nb:Te = 1:0.31:0.14:0.27, Mo:V:Nb:Te = 1:0.24:0.13:0.27, and Mo:V:Nb:Te = 1:0.22:0.12:0.27 as discussed in Chapter 3.1. The high, medium, and low ratio were named by the ratio of V/Mo. The trends of the effect of the metal ratio were shown in Figure 5.1.1, Figure 5.1.2, and Figure 5.1.3 for different argon gas calcination temperatures.

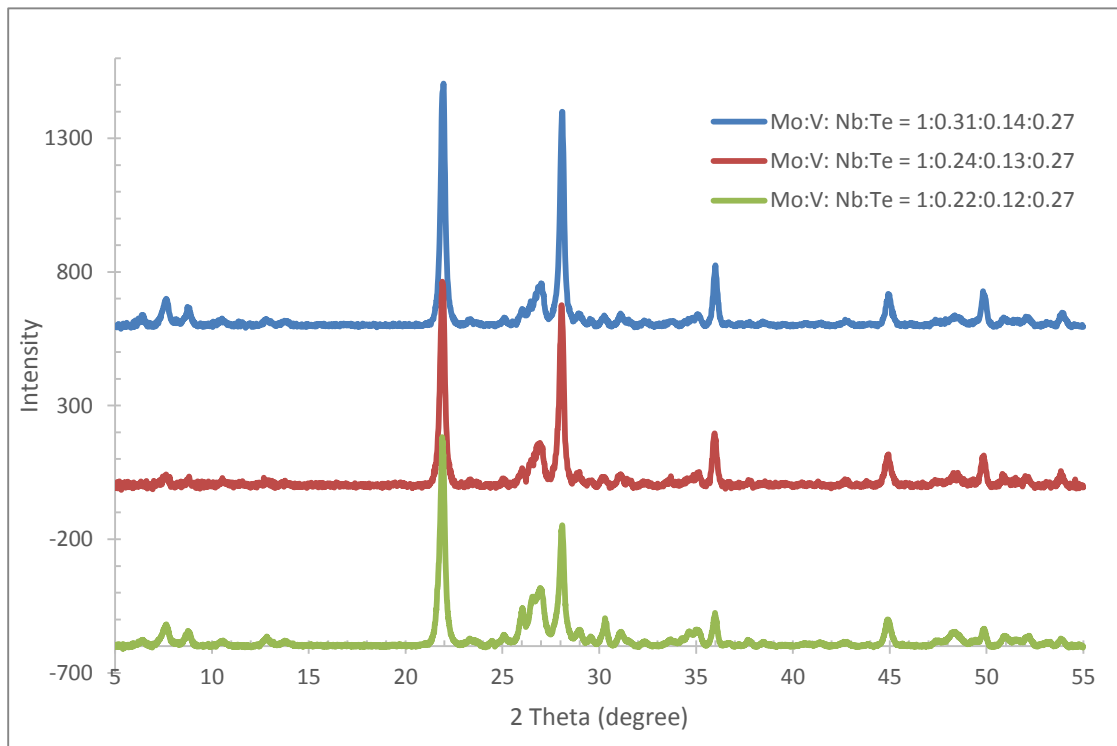


Figure 5.1.1 The X-ray diffraction pattern of metal ratio analysis at 575°C argon calcination temperature (2h argon calcination, XRD setting :4s, 0.02 degree per step, $\lambda=1.5406\text{\AA}$)

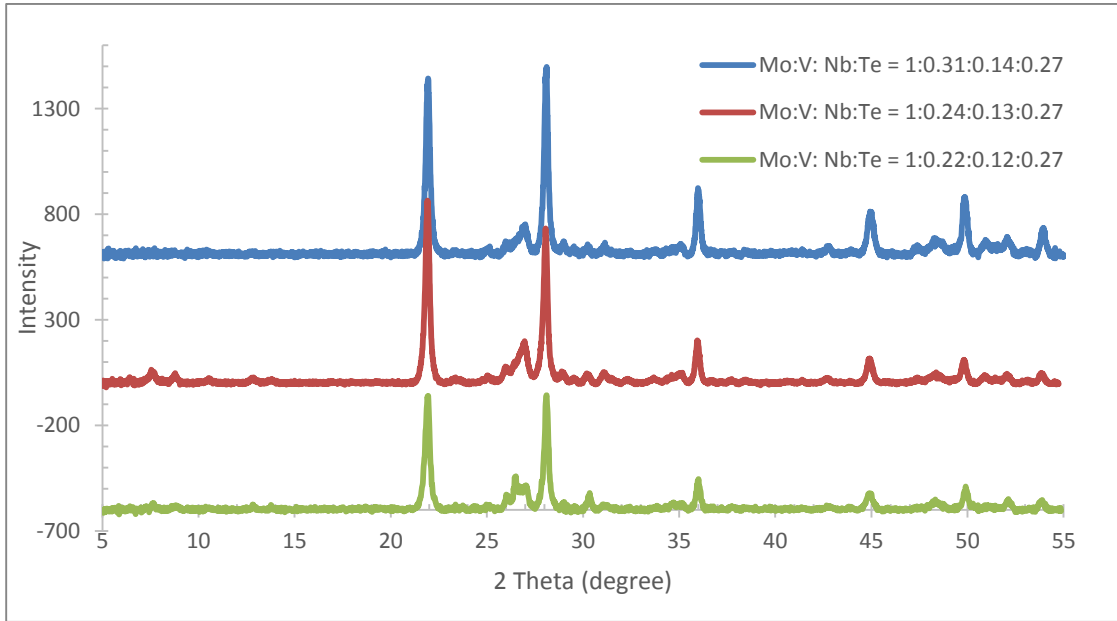


Figure 5.1.2 The X-ray Diffraction pattern of metal ratio analysis at 600°C argon calcination temperature (2h argon calcination, XRD setting :4s, 0.02 degree per step, $\lambda=1.5406\text{\AA}$)

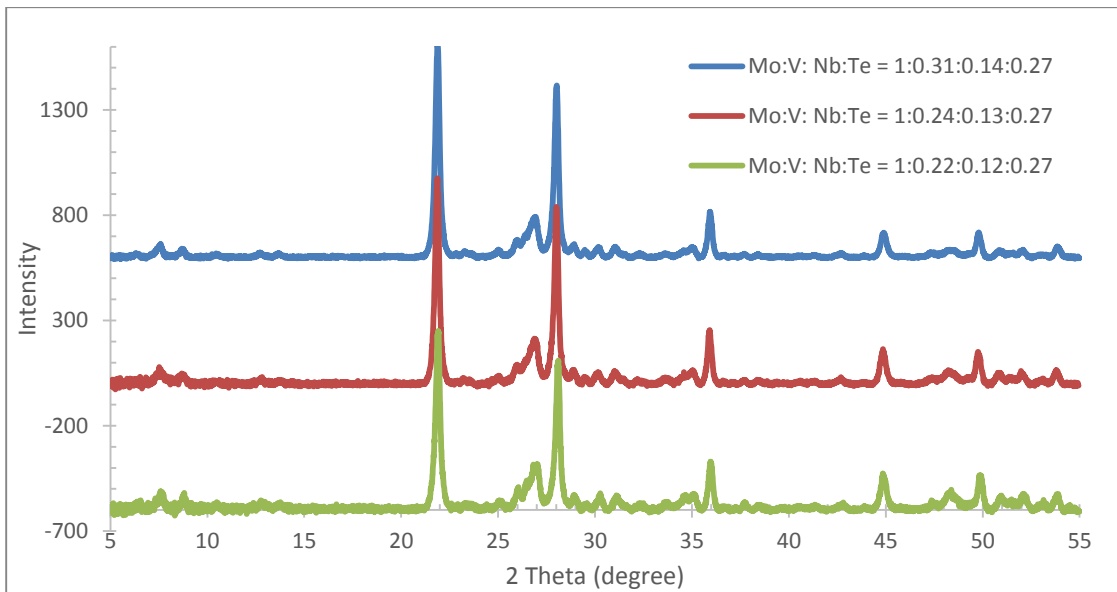


Figure 5.1.3 The X-ray diffraction pattern of metal ratio analysis at 625°C argon calcination temperature (2h argon calcination, XRD setting :4s, 0.02 degree per step, $\lambda=1.5406\text{\AA}$)

The Mo-V-Nb-Te-O *M1* phase catalyst crystallized successfully in all nine samples, and the contaminant, marked in Figure 5.1.4, was found to be *M2* phase. However, it is a “welcome contaminant” when it is in a proportion that is favorable for it to act as a promoter for the active phase, *M1*. The promoter function of *M2* is associated with an improvement in the longevity of the *M1* in its role as a catalyst.

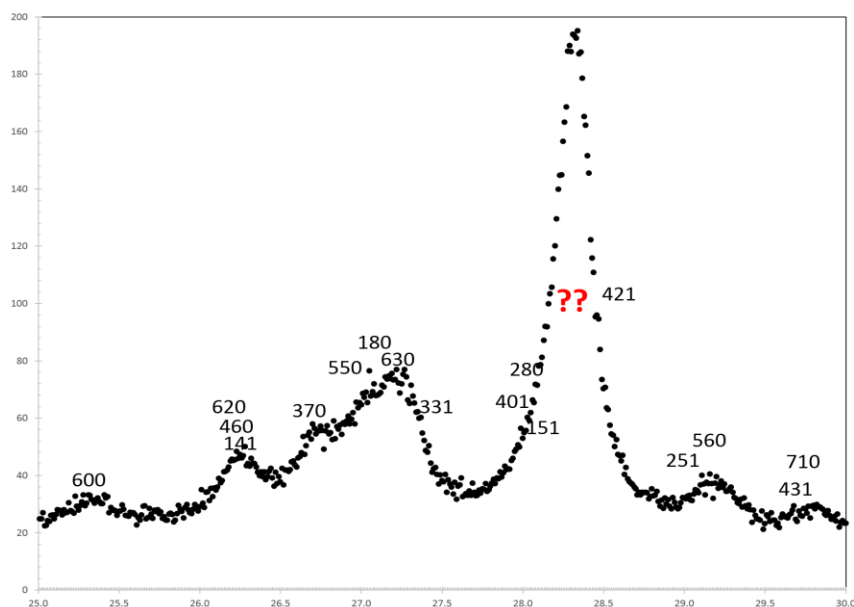


Figure 5.1.4 Expanded section of the X-ray diffraction pattern for the low metal ratio under 625°C argon calcination temperature, selected to show the *M2* phase contaminant. (The intense peak with question mark is (220) peak for *M2* phase structure, and the ratio of *M2/M1* phase was calculated based on that and (001) peak for ratio of *M1* phase.)

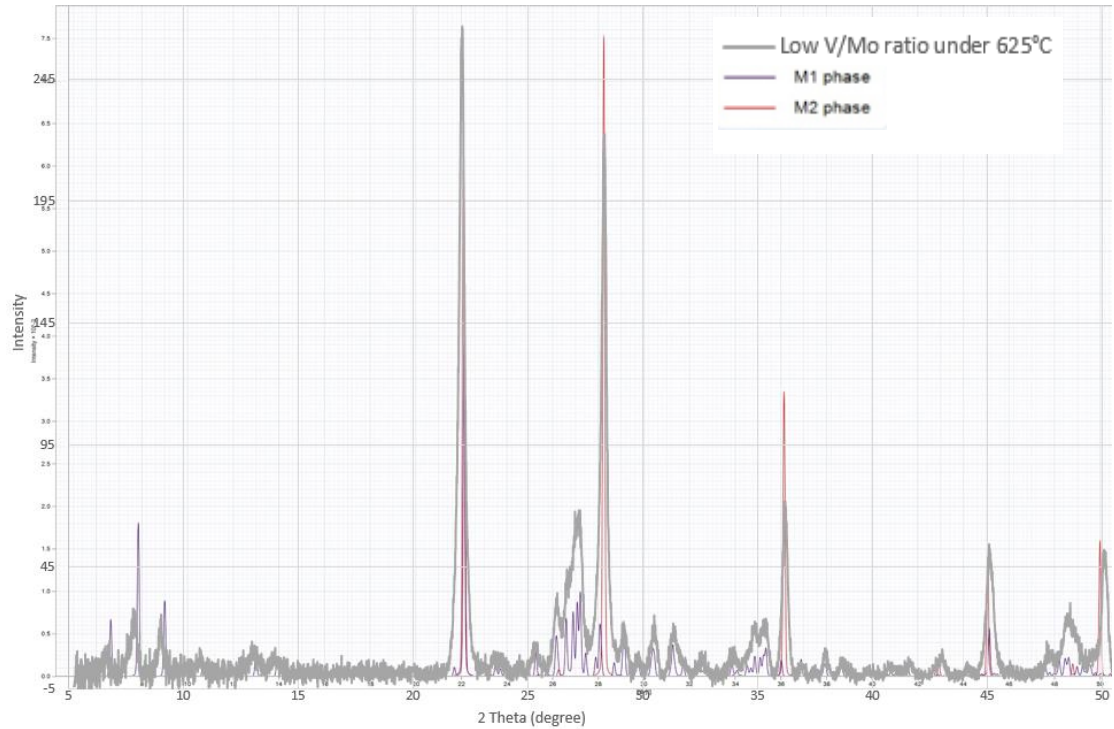


Figure 5.1.5 The example of X-ray diffraction pattern fit for the low metal ratio under 625°C argon calcination temperature.

The ratio of *M2/M1* phase was calculated from the area of intensity at 22.127° (the Bragg's angle for *M1* phase (001) peak) and 28.241° (the Bragg angle for *M2* phase 220 peak) in the X-ray diffraction pattern. The *M2/M1* phase ratio of the three metal ratio sample sets were tabled in Table 5.1.1. This impurity ratio of most samples was about 0.7- 0.8 (*M2/M1* phase). The lower V/Mo ratio crystallized purer *M1* phase than the higher V/Mo ratio one when the V/Mo ratio was within the range of 0.2 to 0.33. The most pure *M1* phase was crystallized from low-ratio reagent combinations, Mo:V:Nb:Te = 1:0.22:0.12:0.27, under 575°C argon calcination temperature. The worst case appeared when the metal ratio was Mo:V:Nb:Te = 1:0.31:0.14:0.27 in combination with 600°C argon calcination. In this case, the M2 content exceed that of

$M1$ on a mole basis. In summary, the trends of $M2/M1$ vary with the change of V/Mo for different calcination temperatures was shown in Figure 5.1.6.

Table 5.1.1 The purity of the Mo-V-Nb-Te-O $M1$ phase catalyst, indicated by the ratio of $M2/M1$, for all three metal ratio sample sets (High, Mo:V:Nb:Te = 1:0.31:0.14:0.27; medium, Mo:V:Nb:Te = 1:0.24:0.13:0.27; low, Mo:V:Nb:Te = 1:0.22:0.12:0.27. The high, medium, and low ratio were named by the ratio of V/Mo).

Argon calcination temperature	$M2/M1$ ratio		
	575°C	600°C	625°C
Low ratio	0.5055	0.8715	0.7197
Medium ratio	0.8486	0.8339	0.8033
High ratio	0.7853	1.0276	0.7493

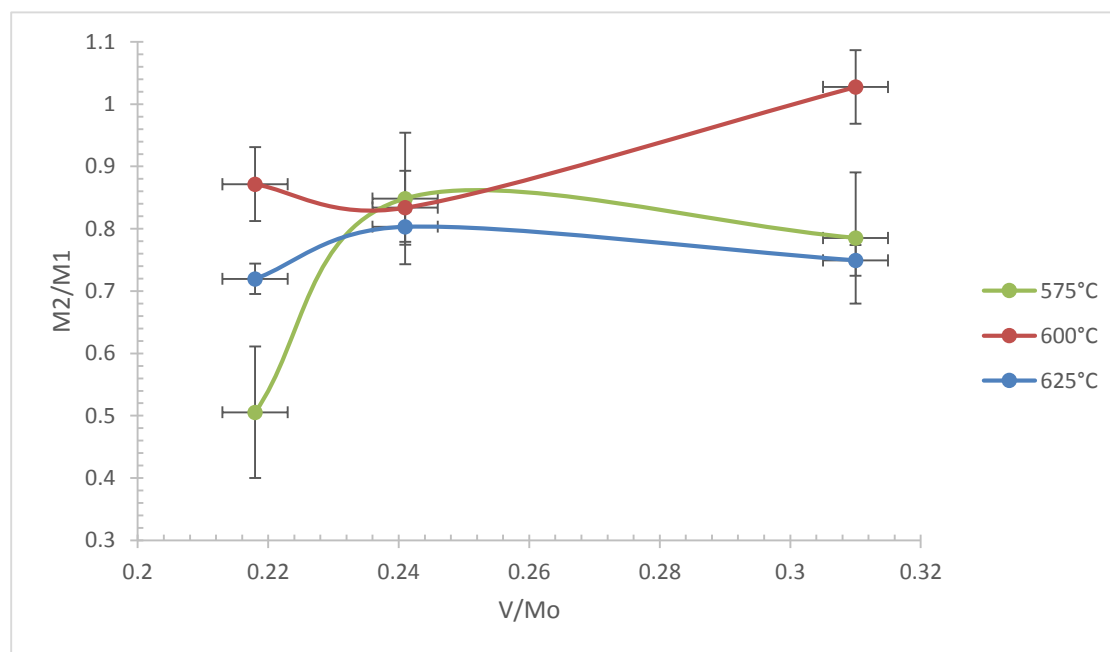


Figure 5.1.6 The influence of metal ratio on the $M2/M1$ ratio under different calcination temperatures.

The size of crystal can be determined from the full width at half maximum by using the Scherrer equation (discussed in Chapter 2.2.5). The FWHM of (600) peaks, (020) peaks, and (001) peaks were used to find the crystal thickness in directions normal to the a, b and c axes, respectively. Additional X-ray diffraction was done at low angles range with 60s and 0.01 degree per step to enhance the statistical confidence in the FWHM determination. Figure 5.1.7 is the X-ray diffraction pattern expanded to show the low angles range for the low metal ratio under 600°C argon calcination temperature, which is used to illustrate the FWHM of (020) peak and calculate the crystal size along the b-axis by Scherrer equation. Since there is significant amount noisy on (020) peak, using the FWHM of (120) peak to estimate the crystal size on b-axis will be more realizable.

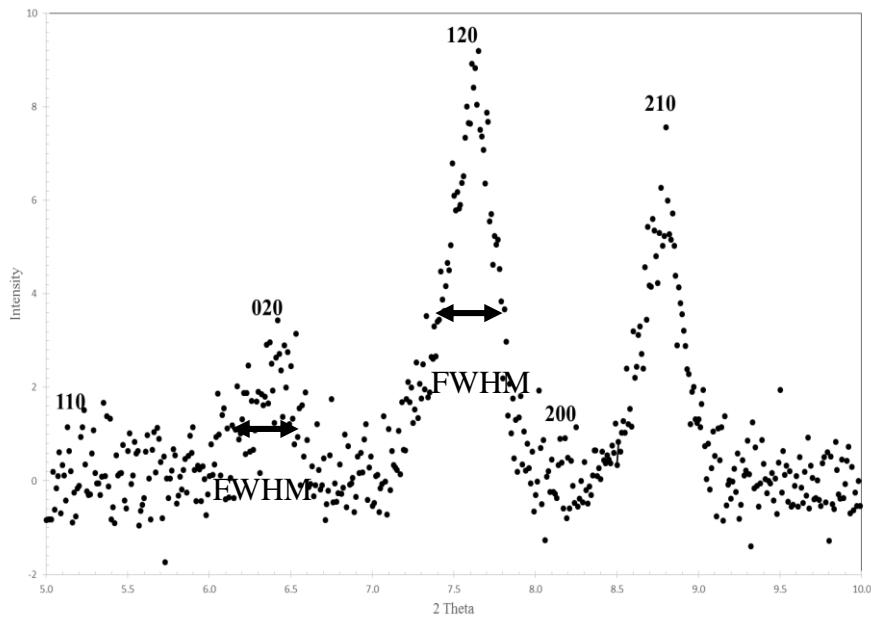


Figure 5.1.7 The X-ray Diffraction pattern at low angle range for the low metal ratio under 600°C argon calcination temperature to show the crystal size was found on each axis. (b-axis as a sample calculation; XRD setting: 60s 0.01 degree per step, $\lambda=1.5406\text{\AA}$)

The comparison of the crystal size for the different metal ratio at the same synthesis condition is shown in Table 5.1.2. The influence of the metal ratio, V/Mo, on the crystal thickness along each dimension, under different argon calcination temperatures, were shown in, Figure 5.1.8, Figure 5.1.9, and Figure 5.1.10. The ratio of *c*-axis to basal plane crystal dimensions for different V/Mo under different calcination temperatures was plotted in Figure 5.1.11. It showed the high ratio of V/Mo tends to crystallize on *c*-axis, and the low ratio one matched my research goal better. Therefore, the Mo:V:Nb:Te = 1:0.22:0.12:0.27 metal ratio was the ratio used for further argon calcination temperature and time mentioned in the next three sections.

Table 5.1.2 The crystal sizes of the three metal ratio sample sets (High, Mo:V:Nb:Te = 1:0.31:0.14:0.27; medium, Mo:V:Nb:Te = 1:0.24:0.13:0.27; low, Mo:V:Nb:Te = 1:0.22:0.12:0.27. The high, medium, and low ratio were named by the ratio of V/Mo.)

Calcination				
Temperature	Metal ratio	t_a axis(Å)	t_b axis(Å)	t_c axis(Å)
575°C	low	189.4	147.8	279.9
	medium	249.5	245.2	313.2
	high	236.3	216.9	314.5
600°C	low	181.2	129.8	285.5
	medium	174.1	443.4	321.5
	high	172.4	---	348.6
625°C	low	187.7	140.0	304.4
	medium	182.6	148.5	327.8
	high	182.3	226.7	335.0

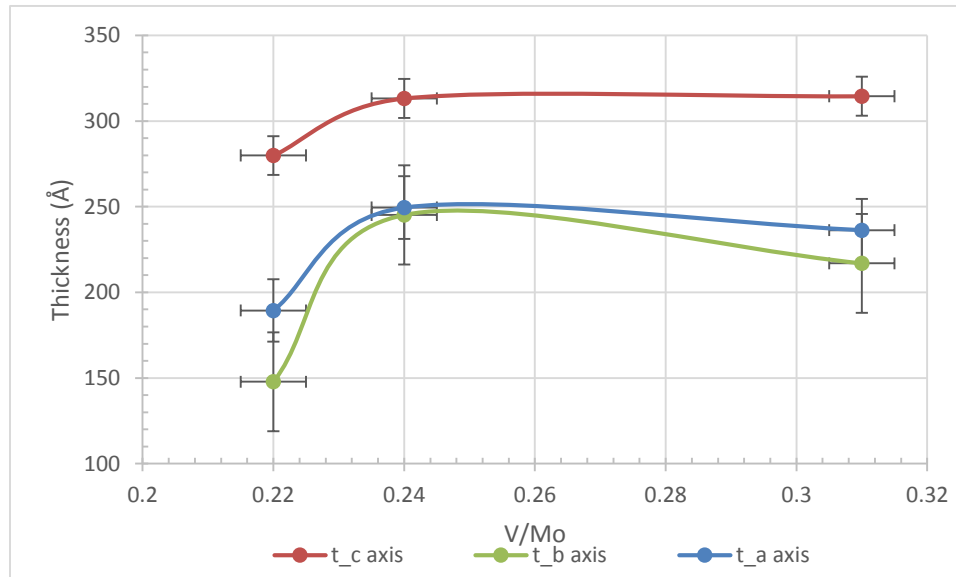


Figure 5.1.8 The influence of metal ratio on the crystal thickness along different directions for the samples calcinated at 575°C

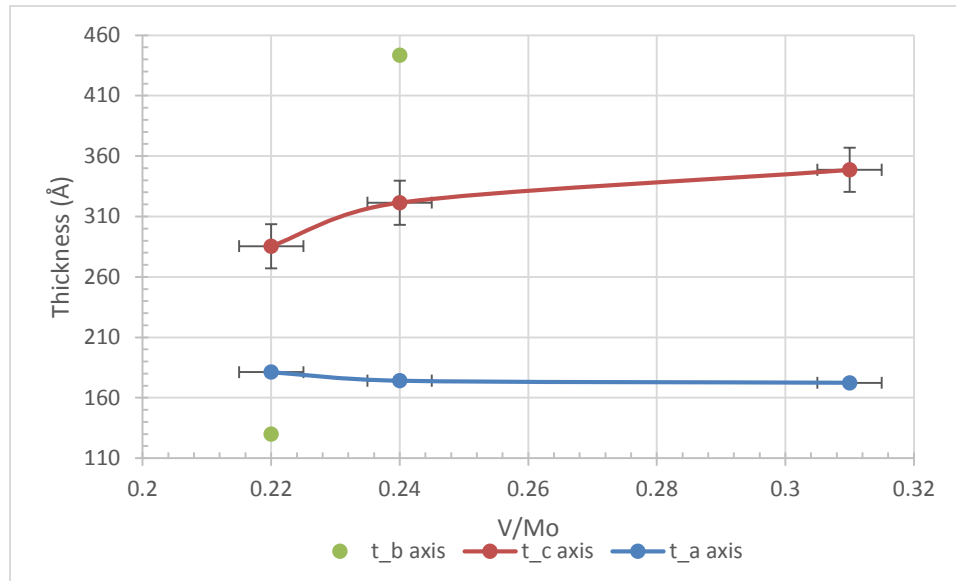


Figure 5.1.9 The influence of metal ratio on the crystal thickness along different directions for the samples calcinated at 600°C

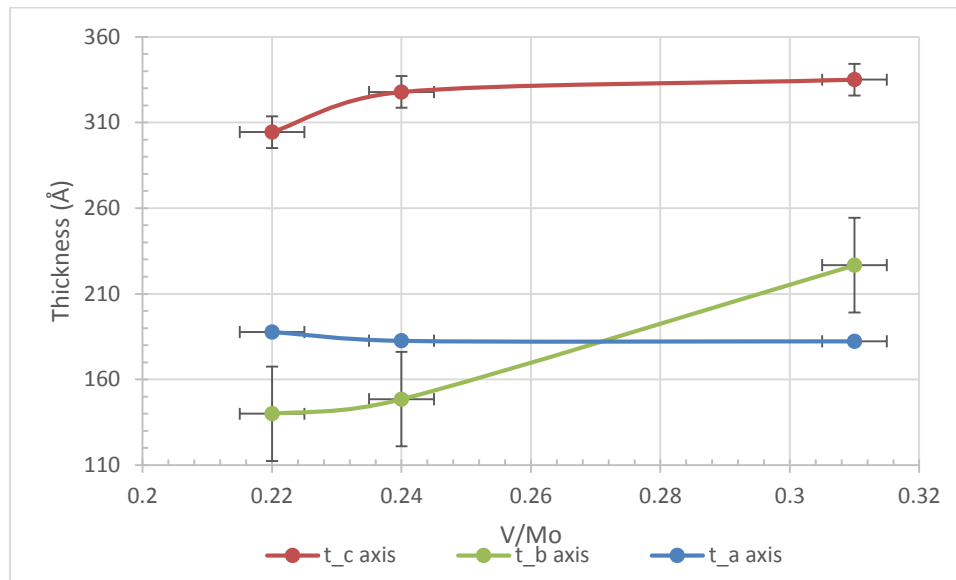


Figure 5.1.10 The influence of metal ratio on the crystal thickness along different directions for the samples calcinated at 625°C

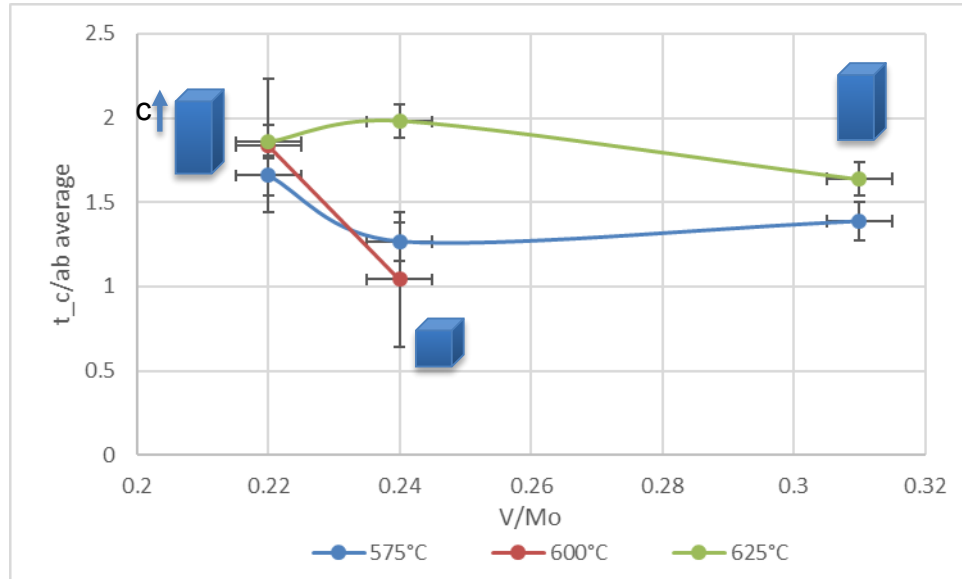


Figure 5.1.11 The ratio of *c*-axis to basal plane crystal dimensions for different V/Mo under different calcination temperatures. The inset prisms depict the relative changes in crystallite morphology.

5.2 Calcination Temperature under Argon Gas

The typical argon gas calcination temperature range for the Mo-V-Nb-Te-O *M1* phase synthesis is from 400 to 600°C [2, 3, 11-22]. Botella et al., Al-Saedi et al., and Pyrz et al. all used the slurry method, in common with the experimental method used for this thesis, and each calcined the Mo-V-Nb-Te-O material at 600°C [11-15]. So, the low, medium, and high V/Mo ratio sample sets were calcined at 600°C with argon gas as a start point. The argon calcination temperature, 575°C and 625°C, were discussed as well. The X-ray diffraction patterns of all three sample sets, with detailed conditions of preparation as shown in Table 4.2.2, were shown in Figures 5.2.1, 5.2.5 and 5.2.6. The corresponding crystal sizes were listed in Tables 5.2.1, 5.2.2, and 5.2.3, respectively. Most of them crystallized into the *M1* phase successfully, and the only contaminant is the *M2* phase. The ratio of *M2*/*M1* phase, calculated from peak

intensities at 22.127° ($M1$) and 28.241° ($M2$) in the X-ray diffraction pattern, as discussed in Section 5.1. The dependence of these $M2/M1$ ratios on preparation conditions was shown in Table 5.1.1.

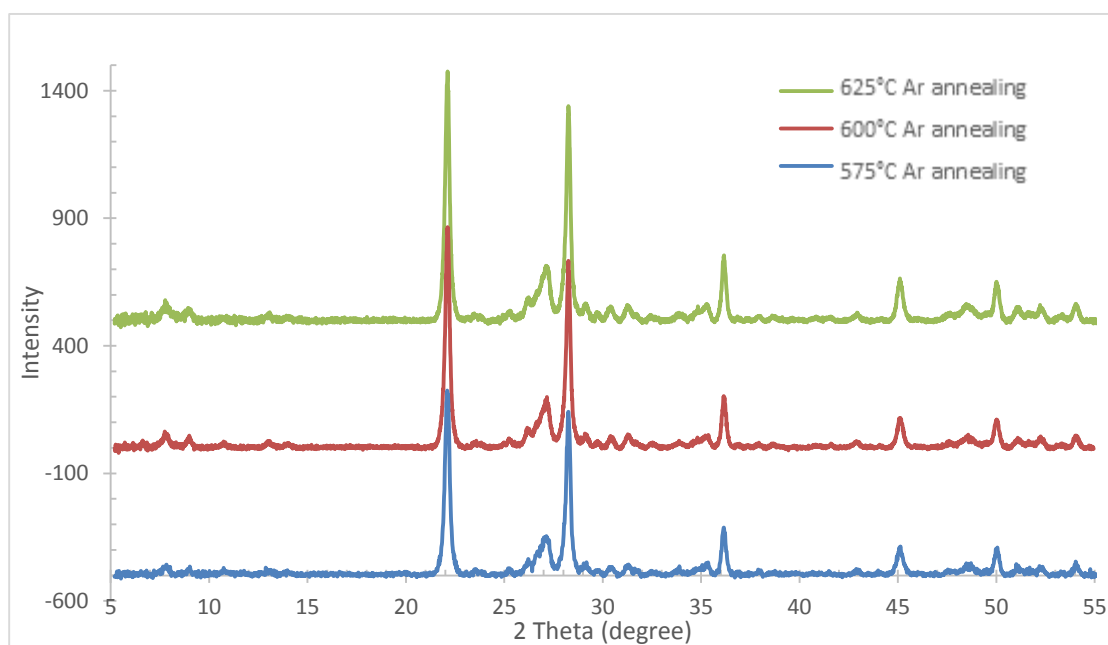


Figure 5.2.1 The X-ray diffraction pattern of the medium V/Mo ratio sample set (2h argon calcination, XRD setting: 4s, 0.02 degree per step, $\lambda=1.5406\text{\AA}$)

All three medium V/Mo ratio samples contain the $M1$ phase, and the only evident contaminant is $M2$. Increasing the argon calcination temperature decreased the purity of $M1$ phase with respect to $M2$, but not significantly. The ratio of $M2/M1$ phase under these three temperatures, as is shown in Figure 5.2.2, were in the range of about 0.80-0.85. From this figure, the trends of $M2/M1$ ratio with the changes of calcination temperature for other V/Mo ratios were also shown.

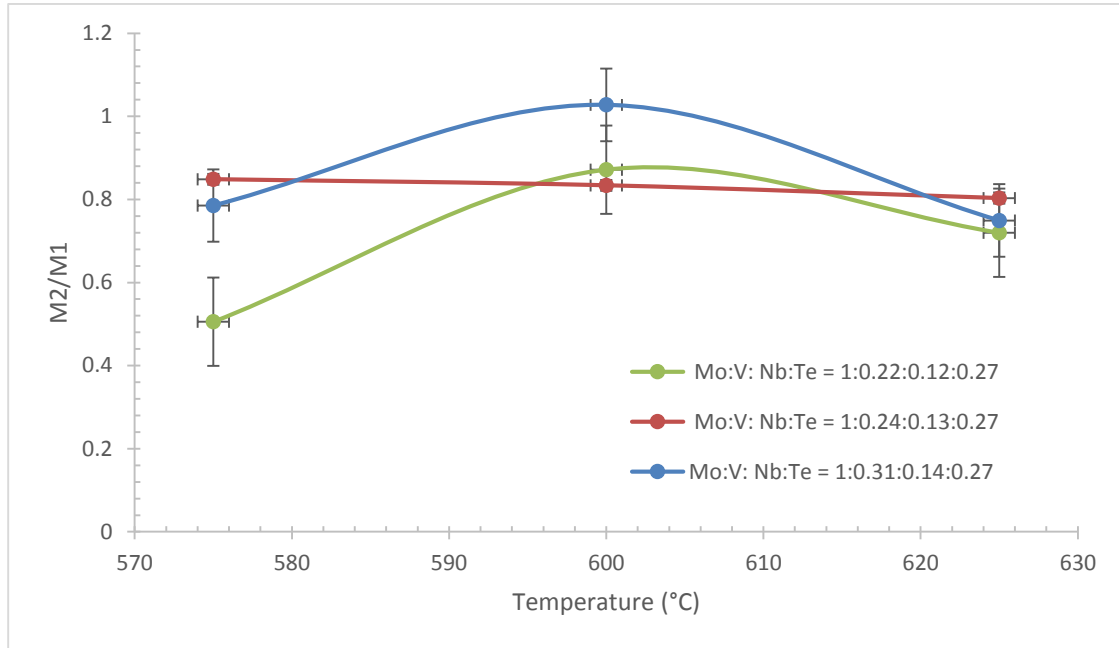


Figure 5.2.2 The trends of $M2/M1$ ratio change with the change of the calcination temperatures for different V/Mo ratio

The crystal dimension along the c -axis were calculated by measuring the FWHM of the (001) reflection for various preparations. These results were tabulated in Tables 5.2.1, 5.2.2, and 5.2.3, and plotted in Figures 5.2.3, 5.2.7, and 5.2.10. The ratios of c -axis to basal plane dimensions for different calcination temperatures with different V/Mo ratios were indicated in Figure 5.2.4.

For three medium V/Mo ratio samples, the sample under 625°C argon calcination had the largest FWHM, and the one calcination at 575°C had the smallest FWHM. Based on the Scherrer equation (mentioned in Chapter 2.2.4), the higher argon calcination temperatures tended to result in larger c -axis dimensions, and the lower temperatures tended to result in a more platy geometry favoring the a - b plane. The anisotropy within the a - b “basal” plane was not of particular concern in this

research. However, lower calcination temperatures tended to produce similar dimensions along the *a*- and *b*-axes, as shown in Tables 5.2.1, 5.2.2, and 5.2.3.

Table 5.2.1 The crystal sizes of the medium V/Mo ratio (Mo:V:Nb:Te = 1:0.24:0.13:0.27) sample sets

Temperature	<i>t</i> _a axis(Å)	<i>t</i> _b axis(Å)	<i>t</i> _c axis(Å)
575°C	249.5	245.2	313.2
600°C	174.1	443.4	321.5
625°C	182.6	148.5	327.8

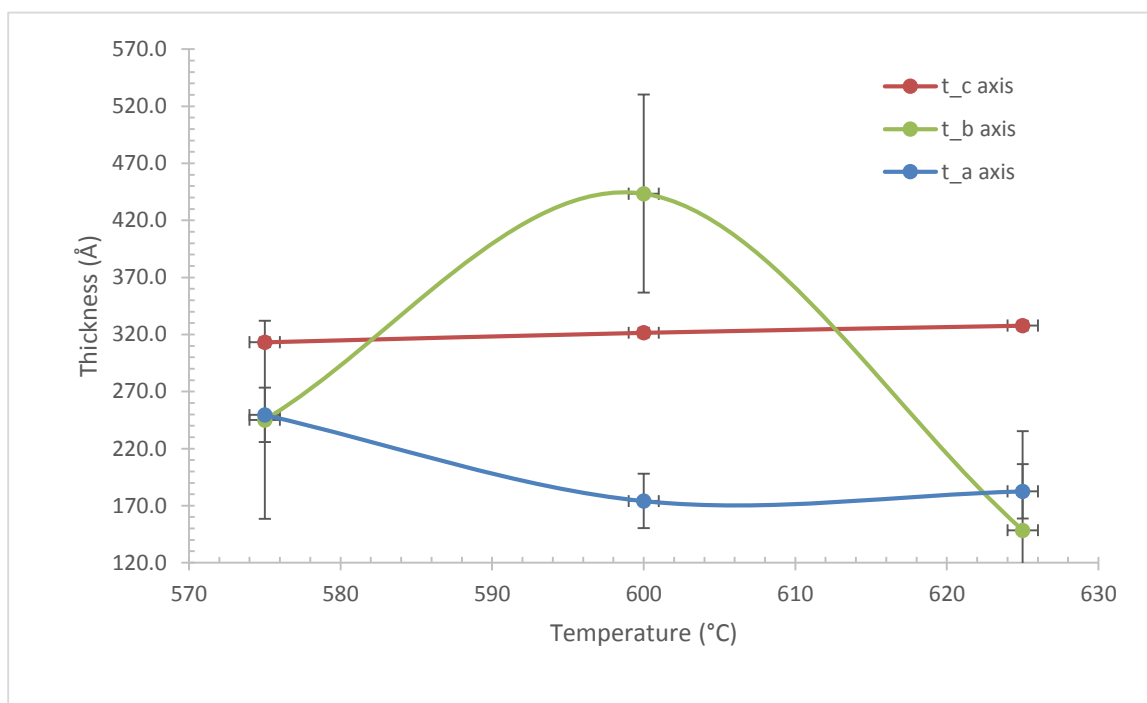


Figure 5.2.3 The influence of argon calcination temperature change on the crystal thickness along different directions for the medium V/Mo ratio sample set.

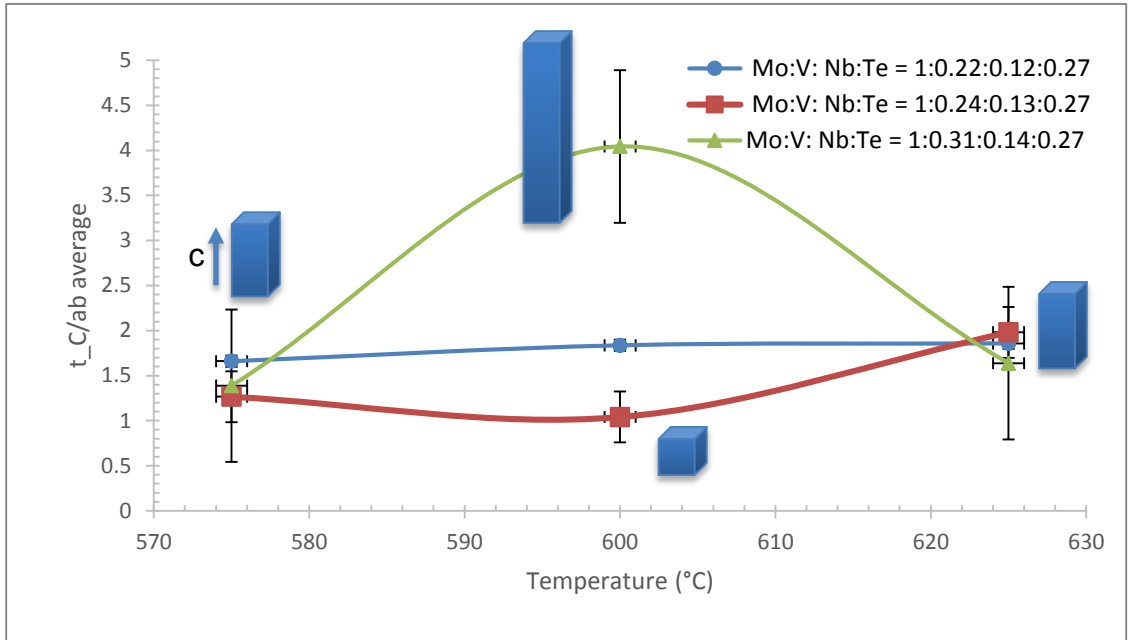


Figure 5.2.4 The *MI* phase crystal size and shape change by temperature for different V/Mo ratio sample sets

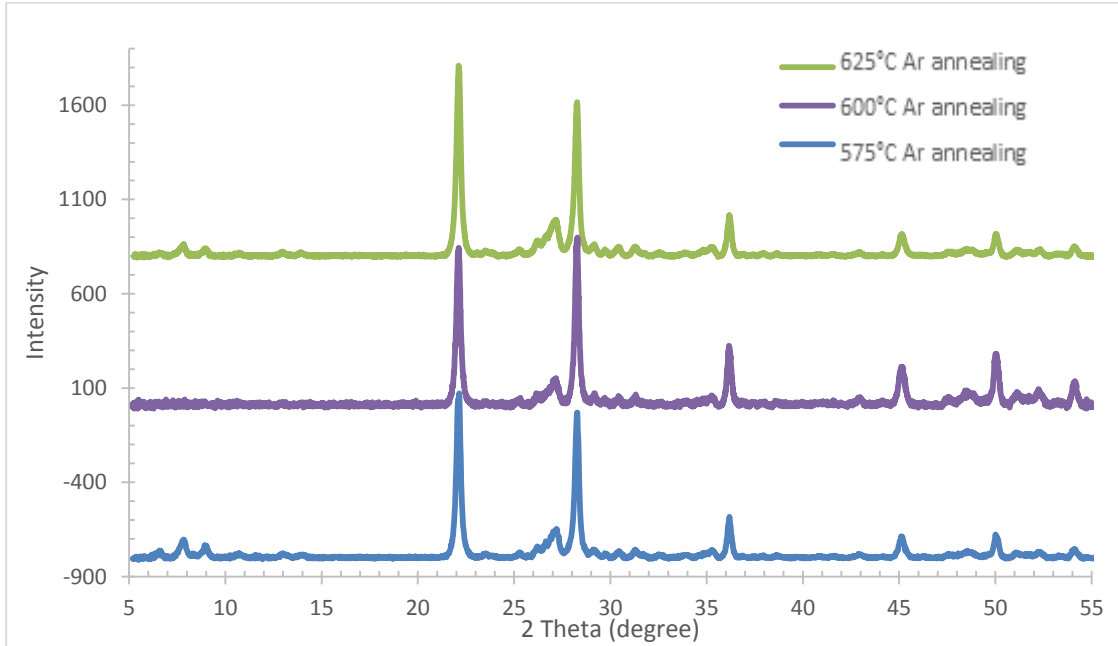


Figure 5.2.5 The X-ray diffraction pattern of the high V/Mo ratio sample set (2 θ argon calcination, XRD setting: 4s, 0.02 degree per step, $\lambda=1.5406\text{\AA}$)

For the high V/Mo ratio sample set, there was no evidence of diffracted intensities in the low-angle range $5^\circ < 2\theta < 10^\circ$ under 600°C argon calcination temperature; therefore, there was no *M1* phase crystallized. It had a significant intensity at $2\theta = 28.241^\circ$, the Bragg angle for *M2* (220) peak, instead; note that this matches the *M2* X-ray diffraction pattern shown in Figure 2.2.1.2. The *M1* phase failed to crystallize under these conditions, but did form under the other two argon calcination temperatures. However, for the low ratio, the crystal size and shape did not change significantly in response to changes in calcination temperature (Figure 5.2.7).

Table 5.2.2 The crystal dimensions of the high V/Mo ratio (Mo:V:Nb:Te = 1:0.31:0.14:0.27) sample sets

Temperature	<i>t</i>_a axis(Å)	<i>t</i>_b axis(Å)	<i>t</i>_c axis(Å)
575°C	236.3	216.9	314.5
600°C	172.4	----	348.6
625°C	182.3	226.7	335.0

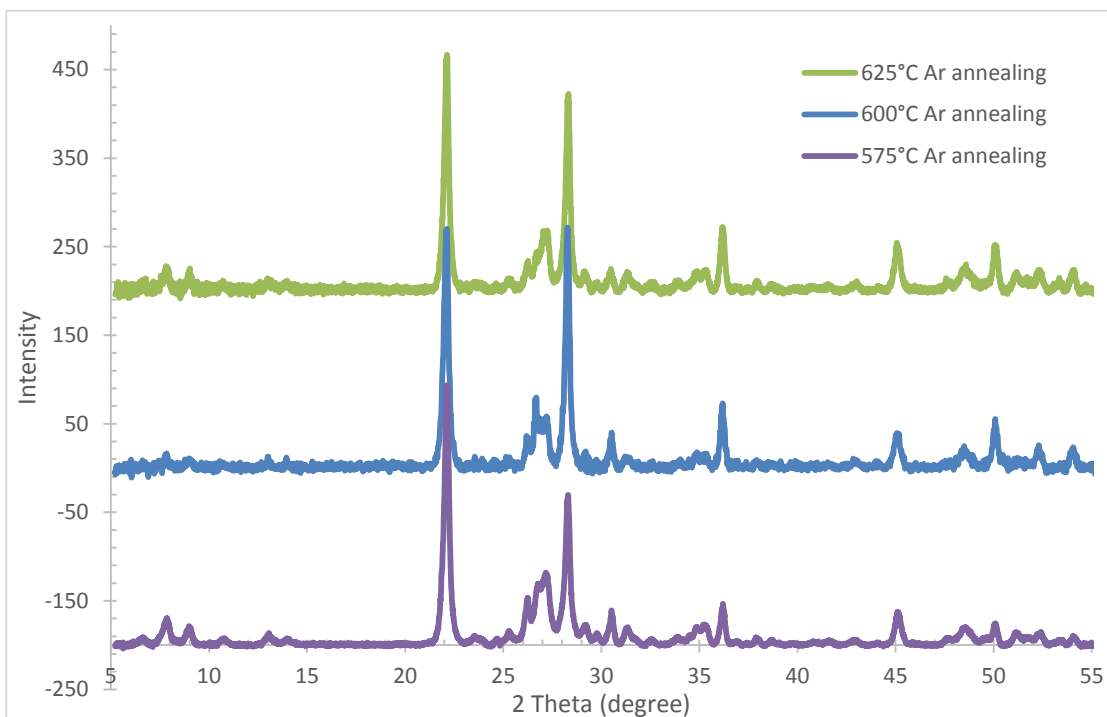


Figure 5.2.6 The X-ray diffraction pattern of the low V/Mo ratio sample set (2h argon calcination, XRD setting: 4s, 0.02 degree per step, $\lambda=1.5406\text{\AA}$)

Table 5.2.3 The crystal sizes of the low V/Mo ratio (Mo:V:Nb:Te = 1:0.22:0.12:0.27) sample sets

Temperature	t_a axis(\AA)	t_b axis(\AA)	t_c axis(\AA)
575°C	189.4	147.8	279.9
600°C	181.2	129.8	285.5
625°C	187.7	140.0	304.4

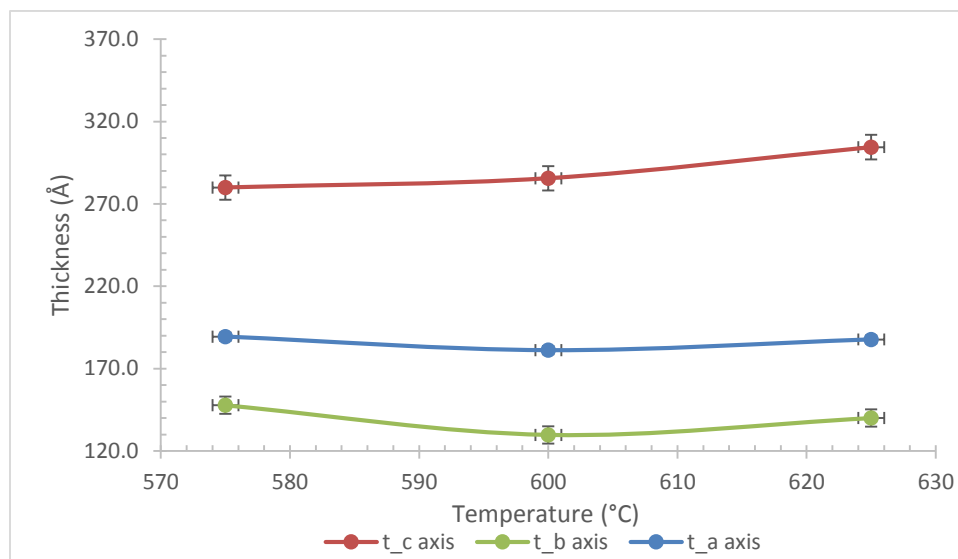


Figure 5.2.7 The influence of argon calcination temperature change on the crystal thickness along different directions for the low V/Mo ratio sample set.

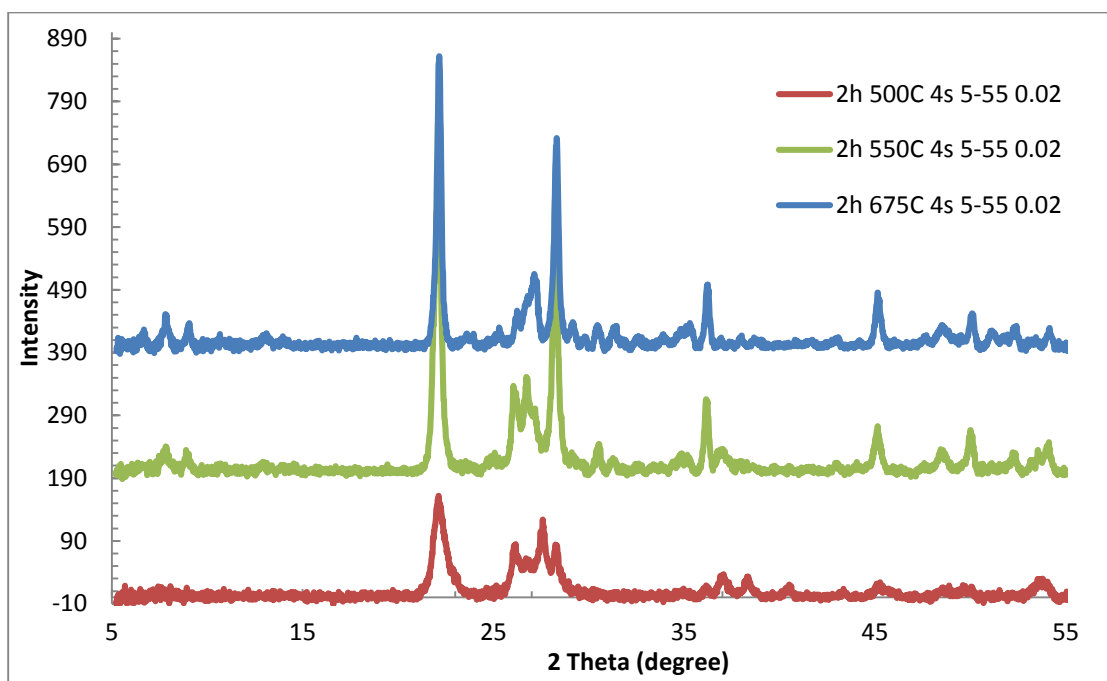


Figure 5.2.8 Sequence of XRD patterns from the various argon treatment temperatures (2h argon calcination, XRD setting: 4s, 0.02 degree step size at $\lambda=1.5406\text{\AA}$).

The bounds on the argon calcination temperature range were determined to be 550-675°C. The ratio of $M2/M1$ was found to reach a maximum near the middle of this range. The ratio of $M2/M1$ at the high calcination boundary, 675°C, was 0.767, and at the lower boundary, 550°C, was 0.716. The sample calcined at 500°C contained no evidence of $M1$; in other words, the multi-peak XRD signature characteristic of $M1$ in the $5^\circ < 2\theta < 10^\circ$ range is not observed. However, since there is a peak at (001), $M1$, $M2$, Mo_5O_{14} , $\text{Mo}_{17}\text{O}_{47}$, or any other phases that have the $c \approx 4.02(2)$ Å lattice constant associated with O-Mo-O layer spacing, might be present, though these would be poorly ordered in the a - b plane with the absence of low angle peaks. It is clear, however, that there is no evidence of well-ordered $M1$ at this temperature. It is possible that there are pentagonal ring subunits that are present, but they would be disordered if the temperature is insufficient for long-range self-assembly as in the example shown by Vogt et al. in Ref [23]. (Figure 5.2.9)

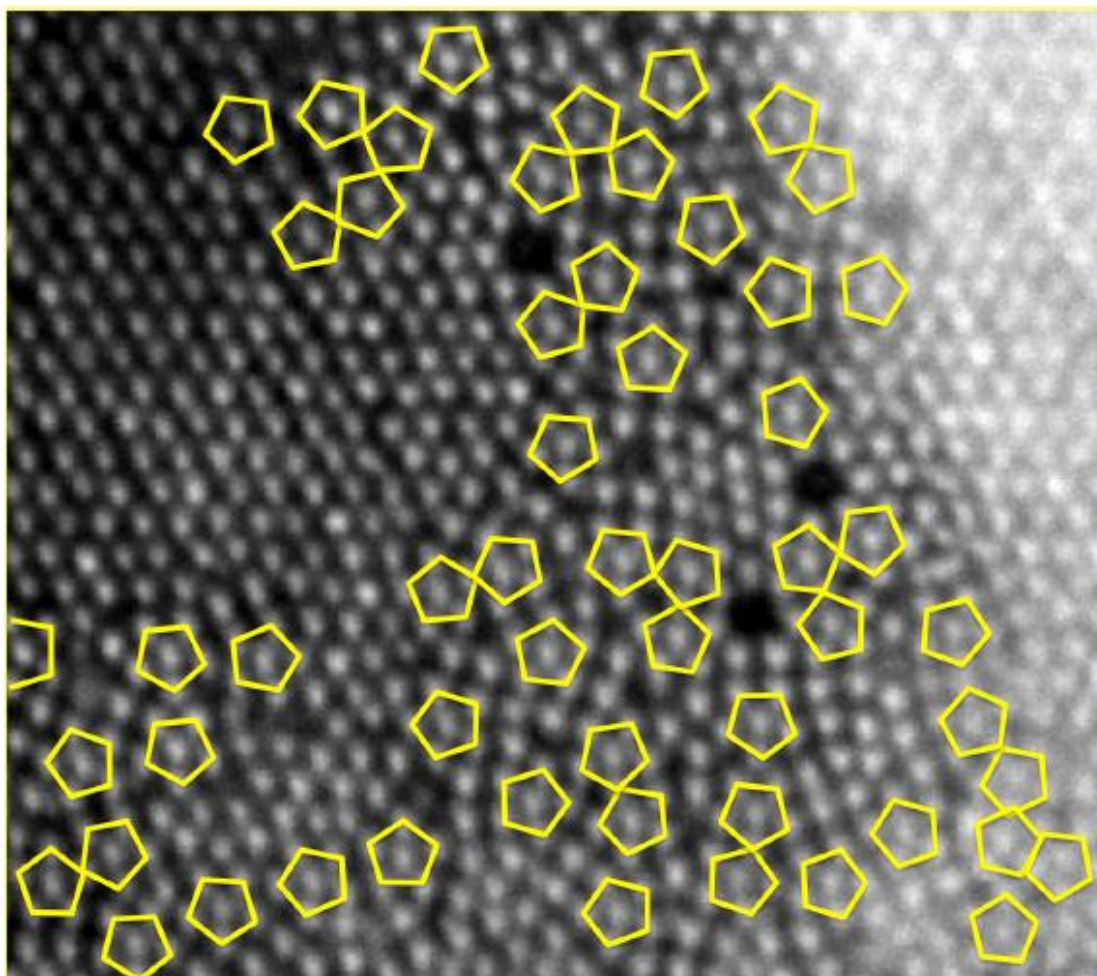


Figure 5.2.9 HAADF-STEM image at 80 kV showing the HTB-type pseudo-hexagonal *M2* domain bounded by a region with substantial disorder within which pentagonal building blocks are found, some of which are conjoined as pairs, triplet, and quadruplets, as marked in yellow.²³

Table 5.2.2 The correlation between crystallite dimensions and calcination temperature for the low-range metal ratio specimens.

Temperature	<i>t</i> _a axis(Å)	<i>t</i> _b axis(Å)	<i>t</i> _c axis(Å)
500°C	82.2	----	114.3
550°C	86.5	81.3	273.8
675°C	168.1	172.1	316.7

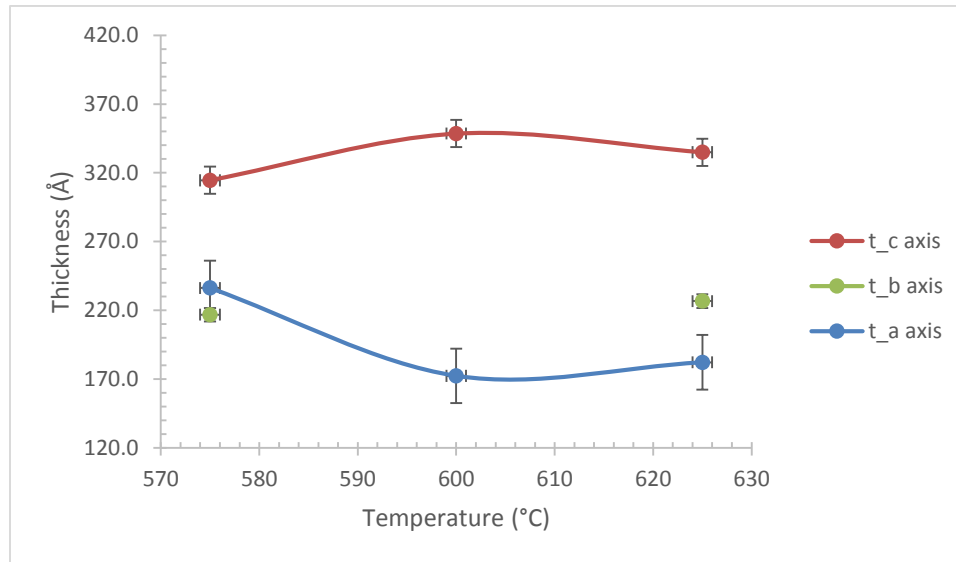


Figure 5.2.9 The influence of argon calcination temperature on the crystallite dimensions.

5.3 Argon Calcination Time

The argon calcination time had a significant amount of influence on the Mo-V-Nb-Te-O *M1* phase crystallization with in the reasonable argon calcination temperature range, 550-675°C. Extending the time to a few hours helped the *M1* crystallization and reduced the *M2* contaminant. Figure 5.3.1 indicated this trend clearly; however, if the argon calcination temperature is outside of this range, extending the argon calcination time, even by days, still fails to produce evidence of *M1* in the X-ray diffraction pattern (see Figure 5.3.5).

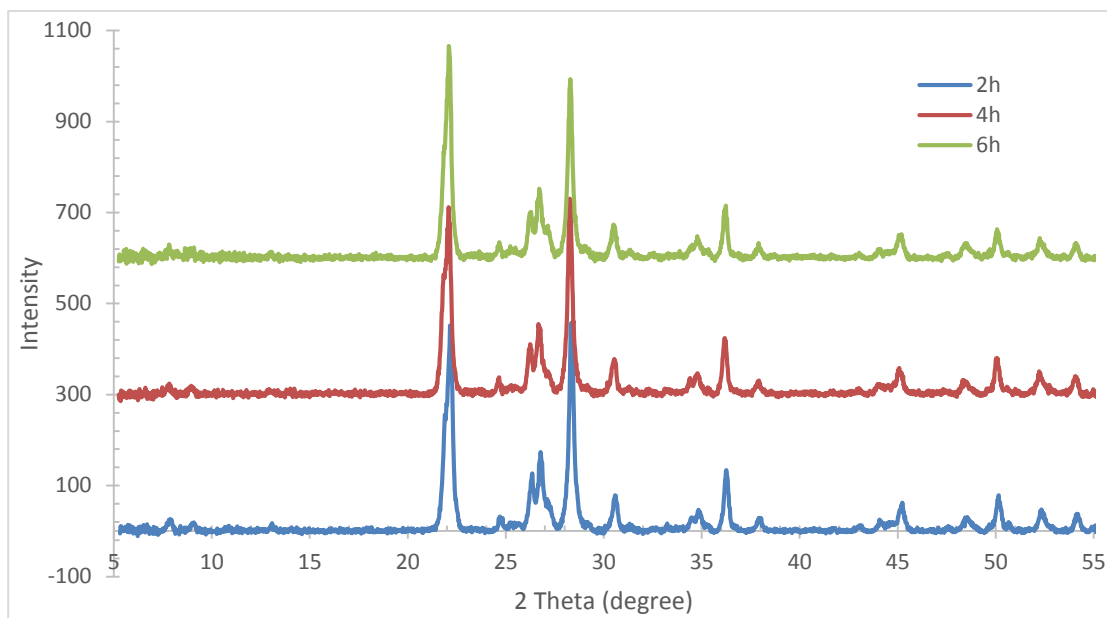


Figure 5.3.1 The X-ray diffraction pattern of the argon calcination time analysis (argon calcination at 625°C, XRD setting: 4s, 0.02 degree per step, $\lambda=1.5406\text{\AA}$)

The trends of the crystallite size and $M2/M1$ ratio with increasing calcination time at 625°C are shown in Figures 5.3.2, 5.3.3, and 5.3.4. As the calcination time increased in this narrow range of 2 – 6 hrs, the $M1$ domain size increased normal to b -axis, but decreased for the a - and c - axis directions. It was found that the ratio of c -axis to basal plane crystal dimensions decreased with time for each of the V/Mo ratios and calcination temperatures. The $M2 / M1$ decreased from 0.866 to 0.641 as the calcination time was increased from 2 to 6 hours. The $M2$ phase appears to have transformed into $M1$ as calcination time increased, which suggests that pentagonal rings formed over time under these conditions. In summary, the mixed phase products crystallized with higher $M1$ content and with larger a - b plane dimensions with longer calcination time.

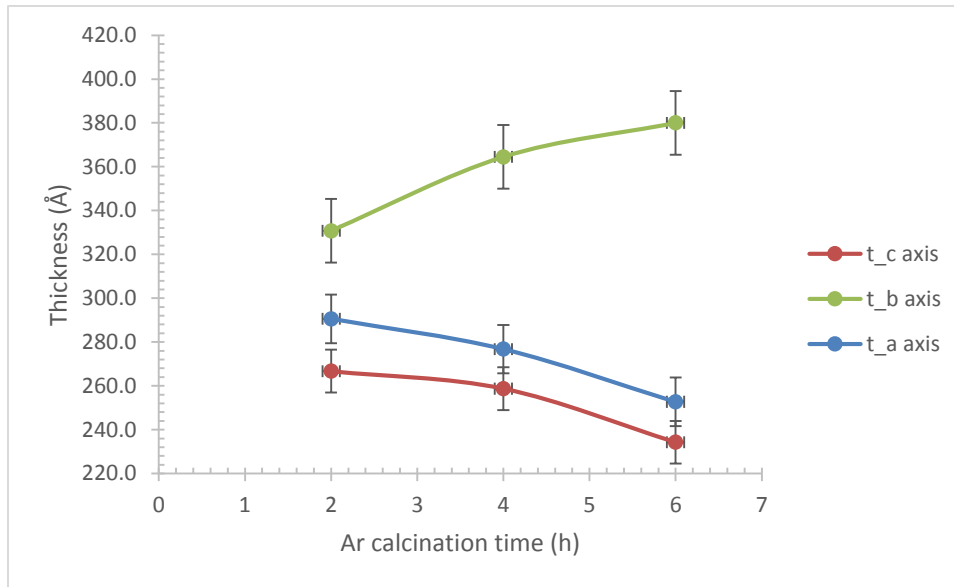


Figure 5.3.2 The influence of calcination time on the crystal thickness along different directions (calcination $T = 625^{\circ}\text{C}$).

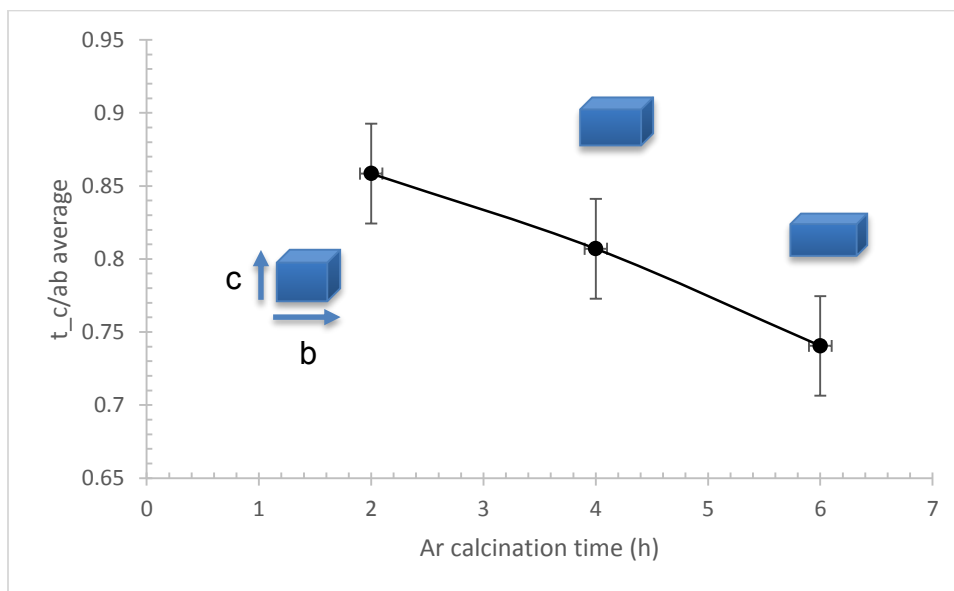


Figure 5.3.3 The *MI* crystallite size and shape dependence on calcination time at $T = 625^{\circ}\text{C}$.

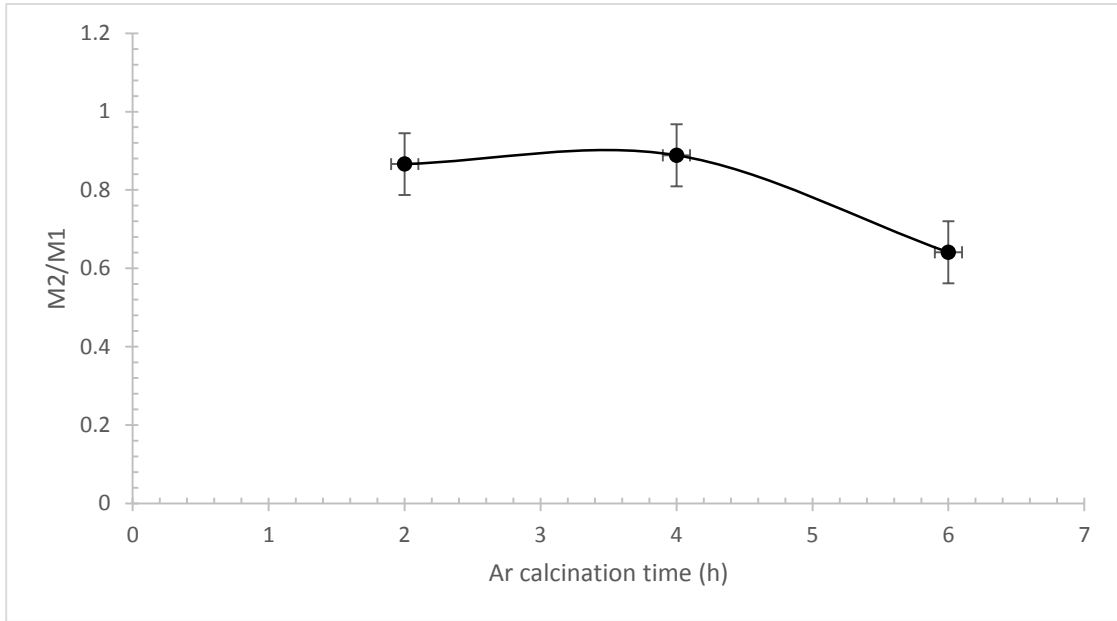


Figure 5.3.4 The trends of $M2/M1$ ratio with increasing calcination time at $T = 625^{\circ}\text{C}$.

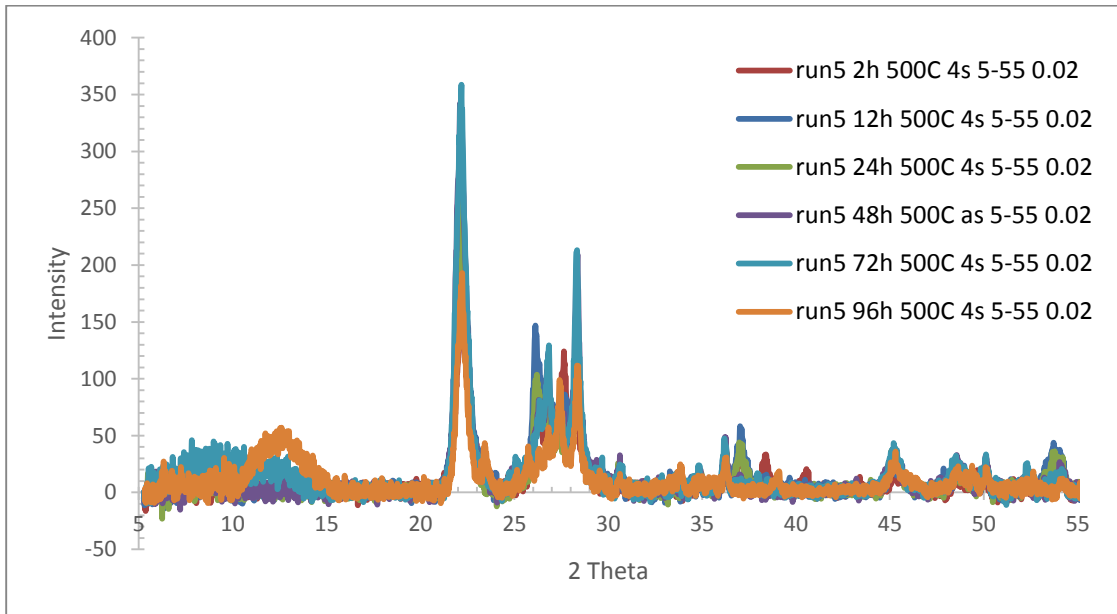


Figure 5.3.5 The comparison of longer calcination time under 500°C argon calcination temperature (XRD setting: 4s, 0.02 degree per step, $\lambda = 1.5406\text{\AA}$).

The X-ray diffraction patterns at 500°C calcination temperature did not show the set of characteristic *MI* reflections expected in the $5^\circ < 2\theta < 10^\circ$ range. However, a peak at 22.127° , characteristic of the (001) reflection of *MI* and other layered Mo-bronzes does appear as a well-formed diffraction peak. A broad feature appeared centered near $2\theta \approx 9.5^\circ$ ($d \approx 9.3 \text{ \AA}$) after 72 hours, and shifted to about $2\theta \approx 12.9^\circ$ ($d \approx 6.9 \text{ \AA}$) after 96 hours. These spacings may indicate a shift from disordered pentagonal rings that are isolated and separated by a single octahedral linkage at 72 hours to conjoined pentagonal rings at 96 hours; however, this would require confirmation using high resolution TEM or STEM imaging. Regardless of the cause of the low-angle features in these patterns, the presence of some diffraction peaks at high angle without low-angle reflections does suggest that significant disorder exists, at least in some dimensions at 500°C. More study of the influence of long calcination times at 500°C will be required to more fully characterize this low temperature behavior.

5.4 pH of the solution

The *MI* phase has been reported to be stable only within a limited pH range, roughly characterized as 2.8-3.2 [16, 20, 24- 26]. Experiments carried out for this thesis study indicated that aqueous stage solutions that are overly acidic or basic produced no *MI* product after calcination. For low V/Mo ratio samples, acidic solutions with pH at or below 2.8 became sticky during the evaporation. The product adhered tightly to the flask wall and appeared as a lustrous, metallic-like coating which could not be readily removed for analysis. The only low V/Mo sample recovered successfully was the one at pH = 2.75. However, that product became highly sintered after calcination, and could not be ground into powder. The materials synthesized from less acidic conditions ($3.6 < \text{pH} < 4.5$) and the one basic condition

studied (pH = 9.26) had less metallic lustre after drying following the evaporation step. None of these showed XRD evidence of *MI* formation, while pH = 3.52 did result in *MI* crystallization, although with contaminants present (*M2*, Mo₅O₁₄, and other phases).

In addition to the pH = 3.52 preparation, several other preparations in which the pH was left at the natural value also produced *MI* product, as can be seen in the tabulated results in Table 5.4.1 below. From the present research, *MI* phase crystallization habit was found to be very sensitive to the pH of the aqueous precursor solution. The range of pH identified for forming products with evidence of *MI* present was found to be 3.2 < pH < 3.5 for the Mo:V:Nb:Te = 1:0.22:0.12:0.27 sample set. One result, using the natural solution pH, resulted in *MI* formation from a higher V/Mo ratio, and was found to have a pH of 2.8, so lower than for the low V/Mo ratio.

Table 5.4.1 The result of whether *MI* phase was crystallized successfully from the pH analysis

Sample#	Lower pH range			pH limit (boundary)			Higher pH range		
	1	2	3	1	2	3	1	2	3
pH	1.27	1.97	3.23 (original)	3.23	3.35 (original)	3.52	3.32 (original)	4.47	9.26
<i>MI</i> phase	N	N	Y	Disordered	Y	Y	Y	N	N

The higher V/Mo ratio will allow *MI* formation at lower pH. The X-ray powder diffraction for the variable pH sample set was shown in Figure 5.4.1. These generally show *MI*, together with the *M2* phase as a contaminant, formed in the

original solution (pH =3.35), but only disordered *M1* phase, together with *M2*, appeared at pH=3.23. It is interesting to note that this pattern shows a broad feature centered at about $2\theta \approx 12.9^\circ$ ($d \approx 6.9 \text{ \AA}$), very similar to that seen at 500°C after 96 hours, but broader; again this may indicate the presence of conjoined pentagonal rings within a disordered matrix, but may also include isolated pentagonal rings that extend the feature to lower angles. For pH =3.52, Mo_5O_{14} began to crystallize. The X-ray powder diffraction pattern for Mo_5O_{14} , simulated using CrystalDiffract, was shown in Appendix A. By considering all the samples in this research, the acceptable pH range for the solution step is approximately 2.8-3.5, encompassing multiple V/Mo metal ratios.

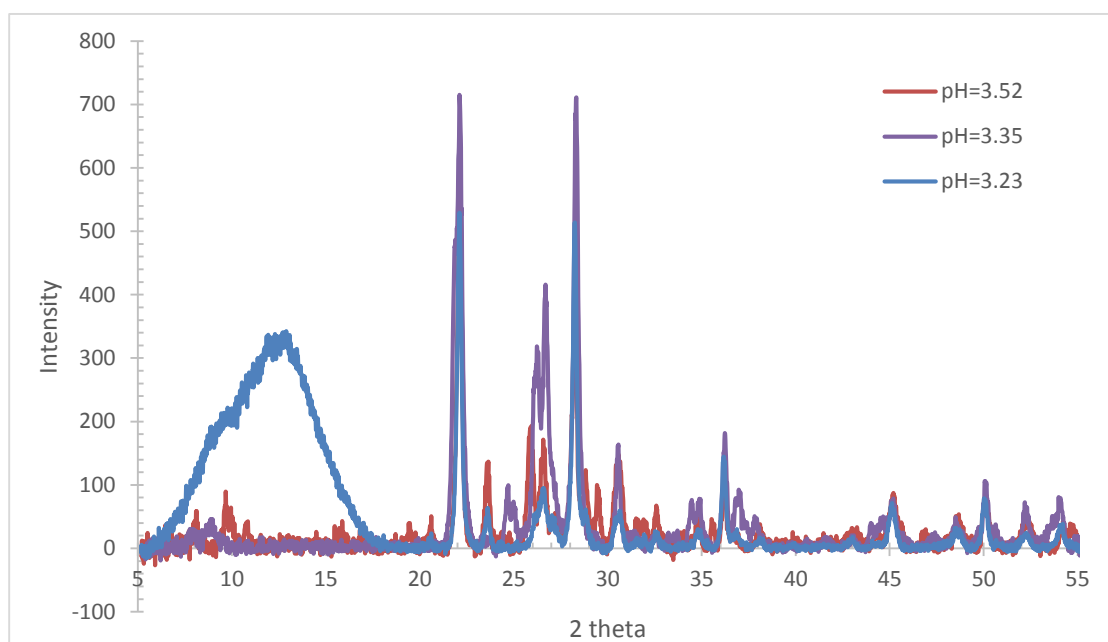


Figure 5.4.1 The X-ray diffraction patterns from the pH dependent study (2h argon calcination at 600°C , XRD setting: 4s, 0.02 degree per step, $\lambda=1.5406\text{\AA}$)

Chapter 6

CONCLUSION

Mo-V-Nb-Te-O mixed-metal oxides were synthesized under a variety of conditions to explore how crystal size and habit are influenced by factors that can be varied during the synthetic process. The starting reagents were ammonium vanadate, ammonium heptamolybdate, ammonium niobium oxalate, and telluric acid, and were used in the slurry method developed by Dr. Xin Li [2,3]. In this work, it was found that the factor that most sensitively influences crystal dimensions of the desired *M1* phase is the temperature; however, the aqueous solution pH strongly influences the phase purity of this product. Other factors, such as the metal ratios, also have some lesser influence the product morphology.

The impurity content in most the samples was Mo-V-Nb-Te-O *M2* phase only; however, this impurity is actually desirable at an appropriate level for its promoter function in improving the longevity of the *M1* phase in its catalyst function. The ratio of *M2/M1* phase, calculated based on the relative intensities of the 22.127° (*M1*) and 28.241° (*M2*) reflections, showed that (i) the lower V/Mo ratio, (ii) longer calcination time, or (iii) either low or high calcination temperature resulted in purer *M1* product, as long as all conditions fall within the recognized reasonable ranges.

From the X-ray diffraction pattern, the Mo-V-Nb-Te-O *M1* phase was confirmed at all calcination temperatures for several different starting compositions, when the natural pH was permitted. Altering the pH typically resulted in no *M1* formation, except in the case of setting pH = 3.52 with low V/Mo ratio. The sensitivity of *M1* formation to the pH is very high. More impurities were observed when the pH was intentionally altered; even small changes in pH result in increased

impurity content. The pH range within which *MI* is stable was found to be 2.8-3.5. This result is different from reports by Young et al., Ishikawa et al., and Ueda et al. [16, 20, 24-26]. Higher V/Mo ratio favored lower pH. Most samples studied had a low V/Mo ratio, set at 0.22, which is close to the lowest metal ratio that can be used to produce *MI*. Further pH dependent studies with other metal ratios within the range 0.20 - 0.33 are recommended for future work.

The useful calcination temperature range was found to be 550 - 675°C. The best condition to obtain *MI* with small *c*-axis dimensions under this research set up was found to be at $T = 550^{\circ}\text{C}$. With the same V/Mo ratio, solution pH, and calcination time, the Mo-V-Nb-Te-O precursors did not crystallize to form the desired *MI* structure at 500°C, at least as evidenced by XRD. It does appear that these low temperature preparation may contain disordered pentagonal rings, possibly conjoined in some cases. Increasing the calcination time up to 96h for this sample did not produce the desired result of creating low-range ordered *MI*; instead it may have created different local organizational arrangements near the atomic level. Calcination temperatures near 550°C and with low metal ratio (V/Mo) resulted in more favorable ratio for the crystallite dimensions in the desired *a-b* plane relative to the *c*-axis. Longer calcination time in argon will result lower *M2/MI* ratio, without changing the *MI* crystallite dimensions significantly.

More research needs to be done with several different factor ranges: (i) higher V/Mo ratios, (ii) calcination temperature in the range 500-550°C, and (iii) to modify pH in order to control the balance of *MI* and *M2* in the product. Also, further analysis on the correlation between composition, annealing time, temperature, and pH, as well

as research on how these factors influence $M2$ coexistence, is the concern moving forward.

REFERENCES

1. Grasselli RK, Burrington JD, Buttrey DJ, DeSanto P, Lugmair CG, Volpe AF, Weingand T (2003), Multifunctionality of Active Centers in (Amm)oxidation Catalysts: from Bi-Mo-O_x to Mo-V-Nb-(Te,Sb)-O_x. *Top. Catal.* 23:5-22
2. Li X, Buttrey DJ, Blom DA, Vogt T (2011), Improvement of the Structural Model for the *M1* Phase Mo-V-Nb-Te-O Propane (Amm)oxidation Catalyst. *Topics in Catal.* 54:614-626
3. Xin, Li, et al. "Investigation of *M1* phase molybdenum based mixed catalysts for selective oxidation of propane." (2011): Print.
4. Pyrz WD, Blom DA, Sadakane M, Kodato K, Ueda W, Vogt T, Buttrey DJ, Atomic-level imaging of Mo-V-O complex oxide phase intergrowth, grain boundaries, and defects using HAADF-STEM (2010), *Proc Natl. Acad. Sci. USA* 107:6152-6157
5. Grand Opening Ceremony for AN and MMA plants in Thailand | Press Releases | Asahi Kasei. (n.d.). Retrieved from https://www.asahi-kasei.co.jp/asahi/en/news/2012/e130213_1.html
6. Katou T, Vitry D, Ueda W (2004), Structure dependency of Mo-V-O-based complex oxide catalysts in the oxidations of hydrocarbons. *Catal. Today* 91-92:237-240
7. "Acrylic Acid Market Size | Industry Analysis Report, 2022." Market Research Reports & Consulting | Grand View Research, Inc, www.grandviewresearch.com/industry-analysis/acrylic-acid-market.
8. "Global Acrylonitrile (ACN) Market - Growth, Trends and Forecasts (2015-2020) - Reportlinker Review." PR Newswire: Press Release Distribution, Targeting, Monitoring and, www.prnewswire.com/news-releases/global-acrylonitrile-acn-market---growth-trends-and-forecasts-2015-2020---reportlinker-review-300145338.html.
9. DeSanto P, Buttrey DJ, Grasselli RK, Lugmair CG, Volpe AF, Toby BH, Vogt T. (2004), Structural aspects of the *M1* and *M2* phases in MoVNbTeO propane ammoxidation catalysts. *Z Krist* 219:152-165
10. Line Position and line Shape Standard for Powder Diffraction (Silicon Powder), National Institute of Standards & Technology Certificate, Standard Reference Material® 640e.

11. Botella P, Garcia-Gonzalez E, Lopez Nieto JM, Gonzalez-Calbet JM, MoVTeNbO multifunctional catalysts: Correlation between constituent crystalline phases and catalytic performance. *Solid State Sciences*, vol. 7, no. 5, 2005, pp. 507-519.
12. Jammal N, Al-Saeedi, Vijay K, Vasudevan, Vadim V, Gulians, Model bulk Mo–V–Te–O catalysts for selective oxidation of propane to acrylic acid. *Catalysis Communications*, vol. 4, no. 10, 2003, pp. 537-542.
13. Pyrz WD, Blom DA, Vogt T, Buttrey DJ (2008), Direct imaging of the MoVTeNbO *MI* phase using an aberration-corrected high-resolution scanning transmission electron microscope. *Angew. Chem. Int. Ed* 47:2788-2791
14. Oliver JM, Lopez Nieto JM, Botella P, Misud A, "The effect of pH on structural and catalytic properties of MoVTeNbO catalysts." *Applied Catalysis A: General*, vol. 257, no. 1, 2004, pp. 67-76.
15. DeSanto P, Buttrey DJ, Grasselli RK, Lugmair CG, Volpe AF, Toby BH, Vogt T. (2003), Structural characterization of the orthorhombic *MI* phase in MoVNbTeO propane oxidation catalyst *Top Catal* 23:23-38
16. Young Jo B, Seop Kum S, Heup Moon S, "Performance of WO_x-added Mo–V–Te–Nb–O catalysts in the partial oxidation of propane to acrylic acid." *Applied Catalysis A: General*, vol. 378, no. 1, 2010, pp. 76-82.
17. Carreon MA, Guliant VV, Olga Guerrero-Perez M, Banares MA, "Mesoporous mixed Mo–V–Nb oxides for propane ammoxidation." *Catalysis Communications*, vol. 10, no. 4, 2009, pp. 416-420.
18. Hibst H, Rosowski F, Cox G, "New Cs-containing Mo–V⁴⁺ based oxides with the structure of the *MI* phase—Base for new catalysts for the direct alkane activation." *Catalysis Today*, vol. 117, no. 1-3, 2006, pp. 234-241.
19. Yuan L, Bhatt S, Beaucage G, Gulians VV, Mamedov S, Soman RS, "Novel Mesoporous Mixed Nb–M (M = V, Mo, and Sb) Oxides for Oxidative Dehydrogenation of Propane." *The Journal of Physical Chemistry B*, vol. 109, no. 49, 2005, pp. 23250-23254.
20. Seop Kum S, Young Jo B, Heup Moon S, "Performance of Pd-promoted Mo–V–Te–Nb–O catalysts in the partial oxidation of propane to acrylic acid." *Applied Catalysis A: General*, vol. 365, no. 1, 2009, pp. 79-87.

21. Wang, Feng, and Wataru Ueda. "Steric Effect on the Catalytic Performance of the Selective Oxidation of Alcohols Over Novel Crystalline Mo–V–O Oxide." *Topics in Catalysis*, vol. 50, no. 1-4, 2008, pp. 90-97.
22. Naumann d'Alnoncourt R, Cspepei LL, Havecker M, Girgsdies F, Schuster ME, Schlogl R, Trunshke A, "The reaction network in propane oxidation over phase-pure MoVTaNb *M1* oxide catalysts." *Journal of Catalysis*, vol. 311, 2014, pp. 369-385.
23. Vogt, T., Blom, D. A., Jones, L., & Buttrey, D. J. (2016). ADF-STEM Imaging of Nascent Phases and Extended Disorder Within the Mo–V–Nb–Te–O Catalyst System. *Topics in Catalysis*, 59(17-18), 1489-1495. doi:10.1007/s11244-016-0665-0
24. Ishikawa, S., Kobayashi, D., Konya, T., Ohmura, S., Murayama, T., Yasuda, N., ... Ueda, W. (2015). Redox Treatment of Orthorhombic Mo₂V₁₁O₁₂ and Relationships between Crystal Structure, Microporosity and Catalytic Performance for Selective Oxidation of Ethane. *The Journal of Physical Chemistry C*, 119(13), 7195-7206. doi:10.1021/jp512848w
25. Ishikawa, S., Tashiro, M., Murayama, T., & Ueda, W. (2014). Seed-Assisted Synthesis of Crystalline Mo₃VO_x Oxides and Their Crystal Formation Mechanism. *Crystal Growth & Design*, 14(9), 4553-4561. doi:10.1021/cg500661p
26. Popova, G., Andrushkevich, T., Dovlitova, L., Aleshina, G., Chesalov, Y., Ishenko, A., ... Khramov, M. (2009). The investigation of chemical and phase composition of solid precursor of MoVTaNb oxide catalyst and its transformation during the thermal treatment. *Applied Catalysis A: General*, 353(2), 249-257. doi:10.1016/j.apcata.2008.10.060
27. Johan Holmberg, Robert Häggblad, Arne Andersson, A study of propane ammoxidation on Mo–V–Nb–Te-oxide catalysts diluted with Al₂O₃, SiO₂, and TiO₂, *Journal of Catalysis*, Volume 243, Issue 2, 25 October 2006, Pages 350-359, ISSN 0021-9517
28. Robert K. Grasselli, Douglas J. Buttrey, James D. Burrington, Arne Andersson, Johan Holmberg, Wataru Ueda, Jun Kubo, Claus G. Lugmair, and Anthony F. Volpe Jr. (2006). Active centers, catalytic behavior, symbiosis and redox properties of MoV(Nb,Ta)TeO ammoxidation catalysts. *Topics in Catalysis* Vol. 38, Nos. 1–3, July 2006 DOI: 10.1007/s11244-006-0066-x

29. Guliants, V. V., Brongersma, H. H., Knoester, A., Gaffney, A. M., & Han, S. (2006). Surface active sites present in the orthorhombic *MI* phases: low energy ion scattering study of methanol and allyl alcohol chemisorption over Mo–V–Te–Nb–O and Mo–V–O catalysts. *Topics in Catalysis*, 38(1-3), 41-50. doi:10.1007/s11244-006-0069-7
30. Grasselli RK (2002), Fundamental principles of selective heterogeneous oxidation catalysis. *Top Catal* 21:79-88
31. Sadakane M, Watanabe N, Katou T, Nodasaka Y, Ueda W (2007), Crystalline Mo₃VO_x Mixed-Metal Oxide Catalyst with Trigonal Symmetry. *Angew Chem Int Ed* 46:1493-1496
32. Blom DA, Pyrz WD, Vogt T, Buttrey DJ (2009), Aberration-corrected STEM investigation of the M2 phase of MoVNbTeO complex oxidation catalyst. *J Electr Micr* 58:193-198
33. Grasselli RK, Lugmair CG, Volpe AF (2011), Towards an Understanding of the Reaction Pathways in Propane Ammoxidation Based on the Distribution of Elements at the Active Centers of the *MI* Phase of the MoV(Nb,Ta)TeO System. *Top. Catal.* 54:595-604
34. Grasselli RK, Volpe AF (2014), Catalytic Consequences of a Revised Distribution of Key Elements at the Active Centers of the *MI* Phase of the MoVNbTeO_x System. *Top Catal* 57:1124-1137
35. Deniau B, Nguyen TT, Delichere P, Safonova O, Millet, J-MM (2013), Redox State Dynamics at the Surface of MoVTe(Sb)NbO *MI* Phase in Selective Oxidation of Light Hydrocarbons. *Top. Catal.* 56:1952-1962
36. Walther T (2006), A new experimental procedure to quantify annular dark field images in scanning transmission electron microscopy. *J Micr.* 221:137-144
37. Wang ZW, Li ZY, Park SJ, Abdela A, Tang D, Palmer RE (2011), Quantitative Z-contrast imaging in the scanning transmission electron microscope with size-selected clusters. *Phys. Rev. B* 84:073408-1-3
38. Konya T, Katou T, Murayama T, Ishikawa S, Sadakane M, Buttrey D, Ueda W (2013), An orthorhombic Mo₃VO_x catalyst most active for oxidative dehydrogenation of ethane among related complex metal oxides. *Catal. Sci. Technol.* 3:380-387

39. Ishenko EV, Anrushkevich TV, Popova GY, Kardash TY, Ishenko AV, Dovitova LS, Cheslova YA (2014), The structure and catalytic properties of amorphous phase in MoVTeO catalysts for propane ammoxidation. *Appl. Catal. A: Gen* 476:91-102
40. Woo J, Sanghavi U, Vonderheide A, Gulians VV (2016) A study of M1/M2 phase synergy in the MoVTe(Nb,Ta)O catalysts for propane ammoxidation to acrylonitrile. *Appl. Catal. A Gen* 515:179-189

Appendix A

MORE CRYSTAL STRUCTURES AND X-RAY DIFFRACTION PATTERNS

There are more than Mo-V-Nb-Te-O *M1* and *M2* phase are possibly synthesized in my research. All the structures in [001] projection of the possible crystals was exported from the CrystalMaker, and shown in following section. The full range ($0^\circ < 2\theta < 180^\circ$) X-ray Diffraction pattern of the *M1* phase, exported from the CrystalDiffract, was also attached in this section.

A.1 Mo-V-Nb-Te-O *M1* phase

The XRD pattern applied in my research was only from 0° to 55° . However, the XRD pattern on the full range was given from the CrystalMarker, and shown in Figure A.1.1. The main [001] projection of Mo-V-Nb-Te-O *M1* structure was shown in the text. The bond structure within a unit cell are shown in Figure A.1.2.

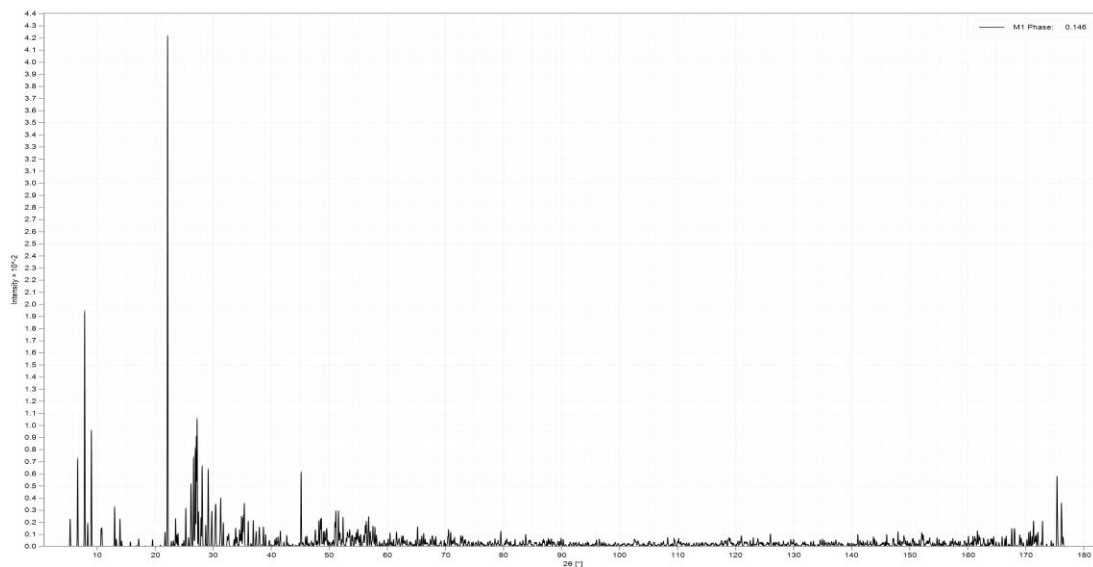


Figure A.1.1 The X-ray diffraction pattern from CrystalDiffract for Mo-V- Nb-Te- O *M1* phase ($0^\circ < 2\theta < 180^\circ$)

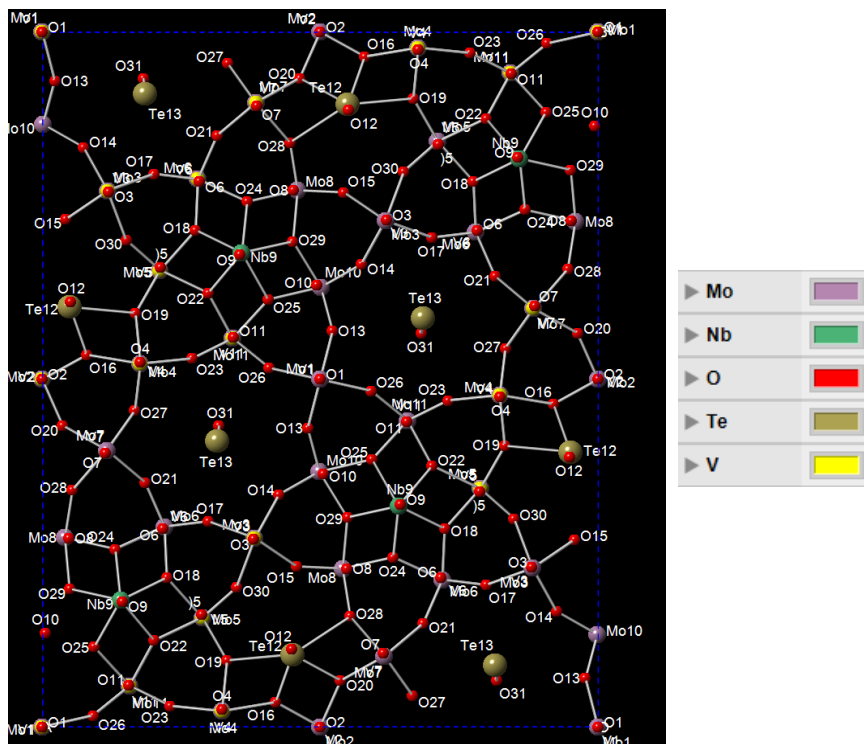


Figure A.1.2 [001] bond structure of the Mo-V-Nb-Te-O *M1* phase catalyst (with labels)

A.2 Mo-V-Nb-Te-O *M2* phase

The main [001] projection of Mo-V-Nb-Te-O *M2* structure was shown in the text. The bond structure within a unit cell are shown in Figure A.2.1.

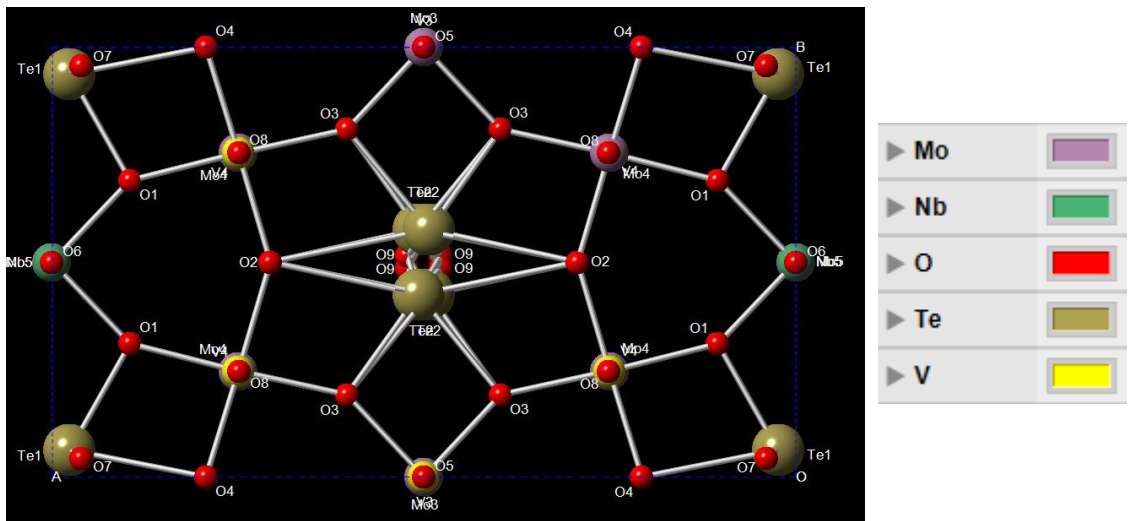


Figure A.2.1 [001] bond structure of the Mo-V-Nb-Te-O *M1* phase catalyst (with labels)

A.3 Mo5O14

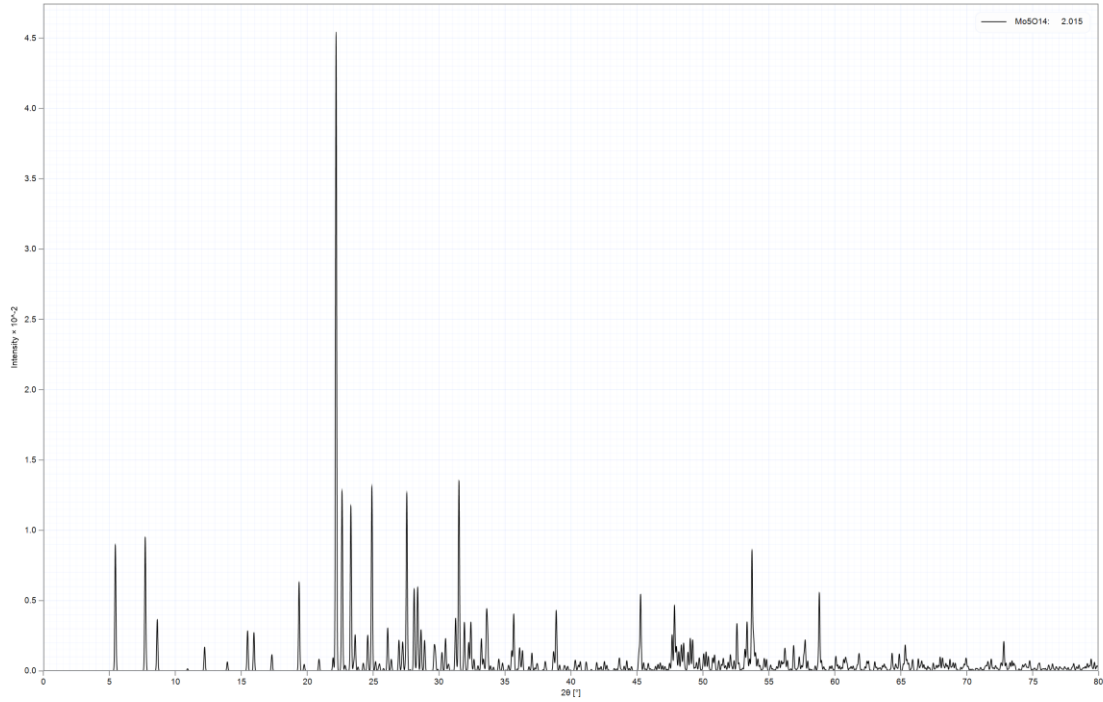


Figure A3.1 The X-ray diffraction pattern from CrystalDiffract for Mo5O14 ($0^\circ < 2\theta < 80^\circ$)

Appendix B

MATLAB CODE

B.1 Pseudo-Voigt approximation

```
x=[0:180];

%% Pesdo Volt
f3=2;
fG=2*f3*(2*log(2))^0.5;
fL=2*f3;
n=0.2 ;
%n=1.36603.*(fL./f)-0.47719.*(fL./f)^2+0.11116.*(fL./f)^3;fL/f=2
%f=(fG.^5+2.69269.*fG.^4.*fL+2.42843.*fG.^3.*fL.^2+4.47163.*fG.^2
.*fL.^3+0.07842.*fG.*fL.^4+fL.^5).^ (1./5)
G=(exp((- (x-80).^2./ (2.*f3.^2))))/(f3.*(2.*pi()).^0.5); %f=10
L=f3./ ((x-80).^2+f3.^2).*pi();
V=n.*L +(1-n).*G;

%% Gaussian
f=0.3.*exp((- (x-80).^2./ (2.*10.^2)));

%% Lorentzian
F=2;
T=0.5*F;
Lz=T./ ((x-80).^2+T.^2).*pi();
plot(x,V,x,f,x,Lz)
xlabel('x');
ylabel('y');
legend('Pesdo-volt','Gaussian','Lorentzian');
```

Appendix C

FWHM FOR SILICON STANDARD

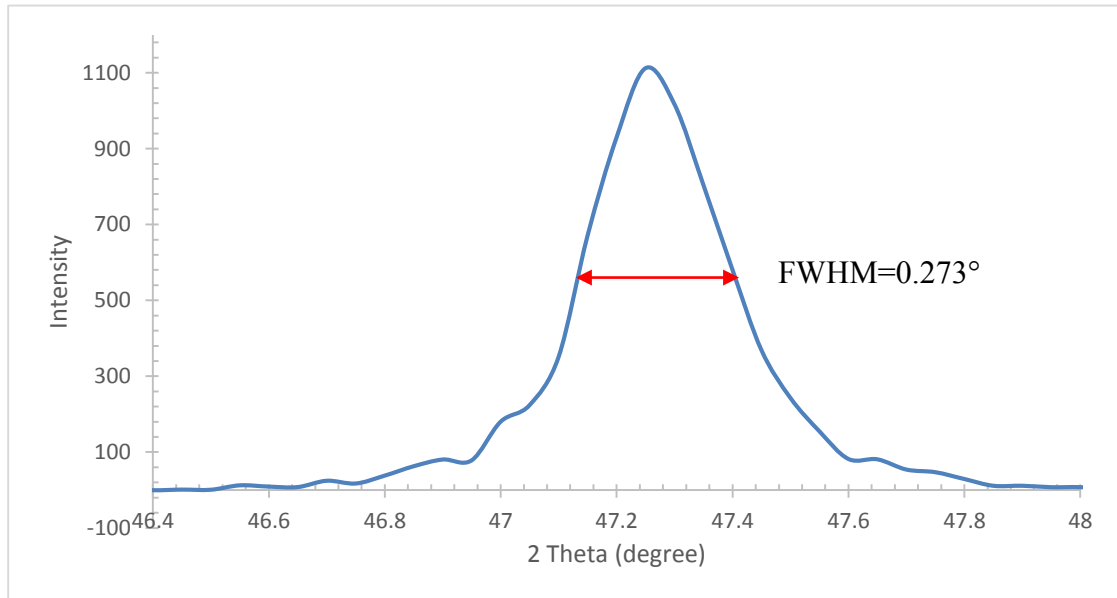


Figure C.1 The zoom in intensity plot with FWHM at 47.300° ($hkl=220$)

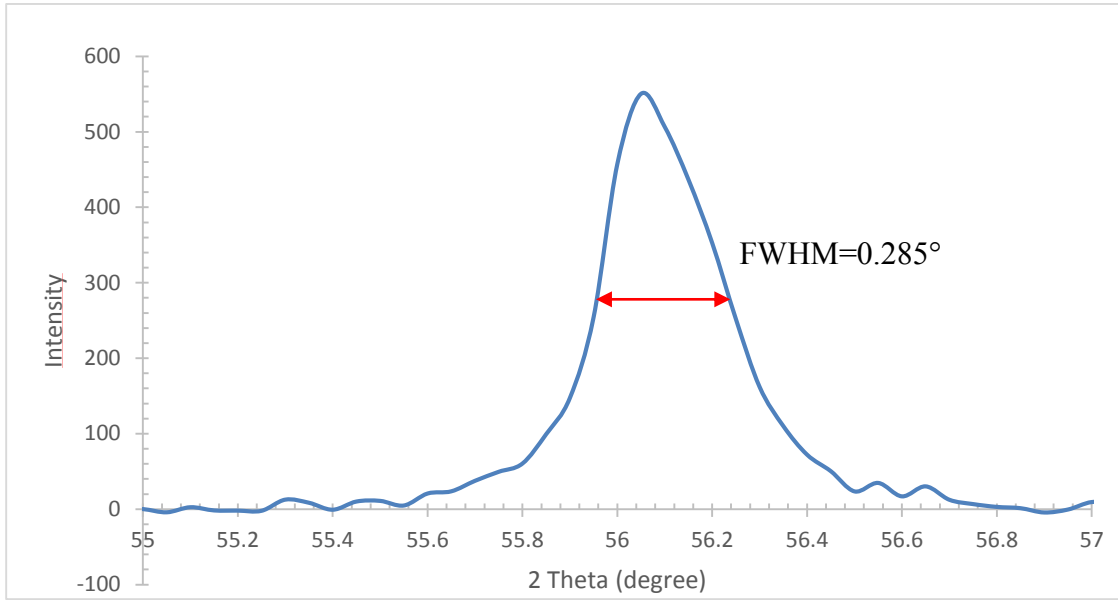


Figure C.2 The zoom in intensity plot with FWHM at 56.120° ($hkl=311$)

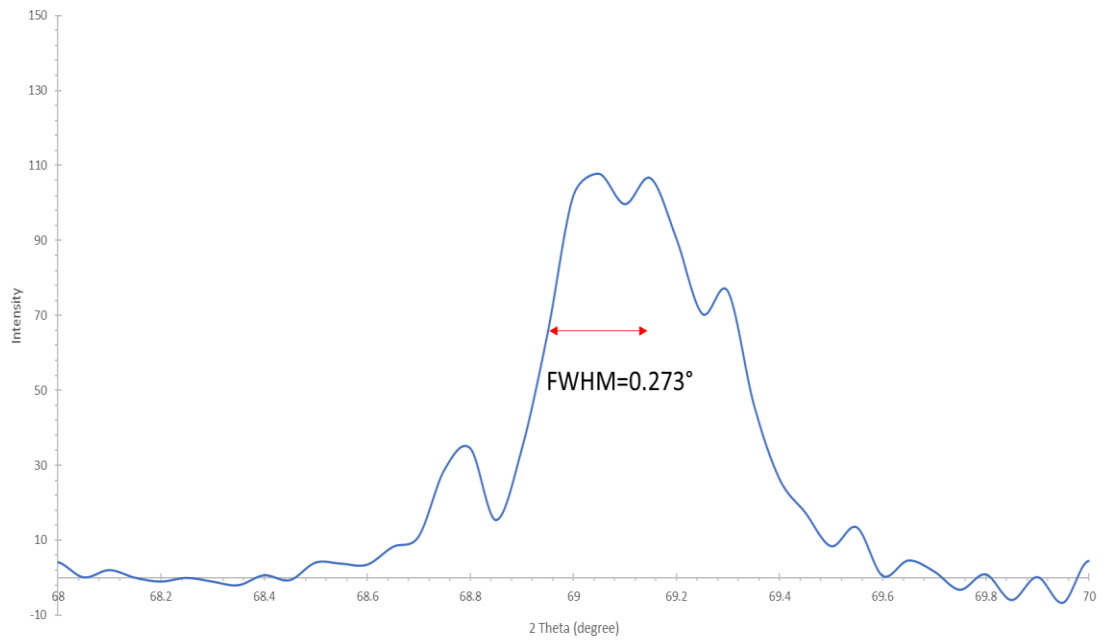


Figure C.3 The zoom in intensity plot with FWHM at 69.126° ($hkl=400$)

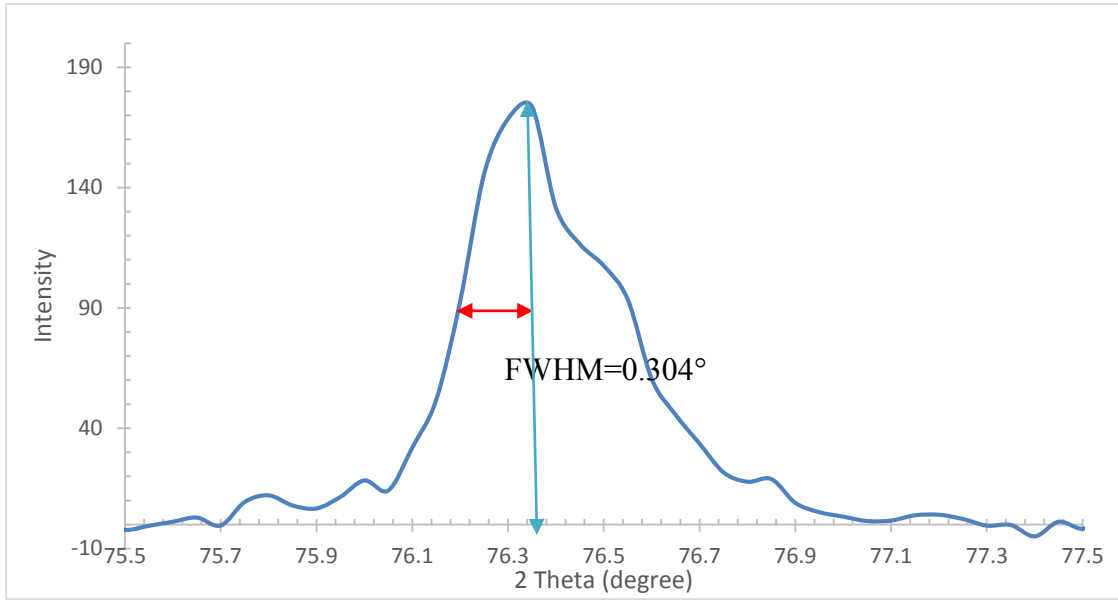


Figure C.4 The zoom in intensity plot with FWHM at 76.372° ($hkl=331$)